

GAMMA-RAY OBSERVATIONS OF THE ORION MOLECULAR CLOUDS WITH THE *FERMI* LARGE AREA TELESCOPE

M. ACKERMANN¹, M. AJELLO², A. ALLAFORT², E. ANTOLINI^{3,4}, L. BALDINI⁵, J. BALLE⁶, G. BARBIELLINI^{7,8}, D. BASTIERI^{9,10},
K. BECHTOL², R. BELLAZZINI⁵, B. BERENJI², R. D. BLANDFORD², E. D. BLOOM², E. BONAMENTE^{3,4}, A. W. BORGLAND²,
E. BOTTACINI², T. J. BRANDT^{11,12}, J. BREGEON⁵, M. BRIGIDA^{13,14}, P. BRUEL¹⁵, R. BUEHLER², S. BUSON^{9,10}, G. A. CALIANDRO¹⁶,
R. A. CAMERON², P. A. CARAVEO¹⁷, C. CECCHI^{3,4}, A. CHEKHTMAN^{18,60}, J. CHIANG², S. CIPRINI^{4,19}, R. CLAUS²,
J. COHEN-TANUGI²⁰, J. CONRAD^{21,22,61}, F. D'AMMANDO^{3,23,24}, A. DE ANGELIS²⁵, F. DE PALMA^{13,14}, C. D. DERMER²⁶,
E. DO COUTO E SILVA², P. S. DRELL², A. DRLICA-WAGNER², T. ENOTO², L. FALLETTI²⁰, C. FAVUZZI^{13,14}, S. J. FEGAN¹⁵,
E. C. FERRARA²⁷, W. B. FOCKE², Y. FUKAZAWA²⁸, Y. FUKUI²⁹, P. FUSCO^{13,14}, F. GARGANO¹⁴, D. GASPARRINI¹⁹, S. GERMANI^{3,4},
N. GIGLIETTO^{13,14}, F. GIORDANO^{13,14}, M. GIROLETTI³⁰, T. GLANZMAN², G. GODFREY², S. GUIRIEC³¹, D. HADASCH¹⁶,
Y. HANABATA²⁸, A. K. HARDING²⁷, M. HAYASHIDA^{2,32}, K. HAYASHI²⁸, D. HORAN¹⁵, X. HOU³³, R. E. HUGHES³⁴, M. S. JACKSON^{22,35},
G. JÓHANNESSEN³⁶, A. S. JOHNSON², T. KAMAE², H. KATAGIRI³⁷, J. KATAOKA³⁸, M. KERR², J. KNÖDLSER^{11,12}, M. KUSS⁵,
J. LANDE², S. LARSSON^{21,22,39}, S.-H. LEE⁴⁰, F. LONGO^{7,8}, F. LOPARCO^{13,14}, M. N. LOVELLETTE²⁶, P. LUBRANO^{3,4}, K. MAKISHIMA⁴¹,
M. N. MAZZIOTTA¹⁴, J. MEHAULT²⁰, W. MITTHUMSIRI², A. A. MOISEEV^{42,43}, C. MONTE^{13,14}, M. E. MONZANI², A. MORSELLI⁴⁴,
I. V. MOSKALENKO², S. MURGIA², T. NAKAMORI³⁸, M. NAUMANN-GODO⁶, S. NISHINO²⁸, J. P. NORRIS⁴⁵, E. NUSS²⁰, M. OHNO⁴⁴,
T. OHSUGI⁴⁷, A. OKUMURA^{2,46}, M. ORIENTI³⁰, E. ORLANDO², J. F. ORMES⁴⁸, M. OZAKI⁴⁶, D. PANEQUE^{2,49}, J. H. PANETTA²,
D. PARENT^{18,60}, V. PELASSA³¹, M. PESCE-ROLLINS⁵, M. PIERBATTISTA⁶, F. PIRON²⁰, G. PIVATO¹⁰, T. A. PORTER², S. RAINÒ^{13,14},
M. RAZZANO^{5,50}, A. REIMER^{2,51}, O. REIMER^{2,51}, M. ROTH⁵¹, H. F.-W. SADROZINSKI⁵⁰, C. SGRÒ⁵, E. J. SISKIND⁵³, G. SPANDRE⁵,
P. SPINELLI^{13,14}, A. W. STRONG⁵⁴, H. TAKAHASHI⁴⁷, T. TAKAHASHI⁴⁶, T. TANAKA², J. G. THAYER², J. B. THAYER², O. TIBOLLA⁵⁵,
M. TINIVELLA⁵, D. F. TORRES^{16,56}, A. TRAMACERE^{2,57,58}, E. TROJA^{27,62}, Y. UCHIYAMA², T. L. USHER², J. VANDENBROUCKE²,
V. VASILEIOU²⁰, G. VIANELLO^{2,57}, V. VITALE^{44,59}, A. P. WAITE², P. WANG², B. L. WINER³⁴, K. S. WOOD²⁶,
Z. YANG^{21,22}, AND S. ZIMMER^{21,22}

¹ Deutsches Elektronen Synchrotron DESY, D-15738 Zeuthen, Germany

² W. W. Hansen Experimental Physics Laboratory, Kavli Institute for Particle Astrophysics and Cosmology, Department of Physics and SLAC National Accelerator Laboratory, Stanford University, Stanford, CA 94305, USA; kamae@slac.stanford.edu, oxon@mac.com

³ Istituto Nazionale di Fisica Nucleare, Sezione di Perugia, I-06123 Perugia, Italy

⁴ Dipartimento di Fisica, Università degli Studi di Perugia, I-06123 Perugia, Italy

⁵ Istituto Nazionale di Fisica Nucleare, Sezione di Pisa, I-56127 Pisa, Italy

⁶ Laboratoire AIM, CEA-IRFU/CNRS/Université Paris Diderot, Service d'Astrophysique, CEA Saclay, F-91191 Gif sur Yvette, France

⁷ Istituto Nazionale di Fisica Nucleare, Sezione di Trieste, I-34127 Trieste, Italy

⁸ Dipartimento di Fisica, Università di Trieste, I-34127 Trieste, Italy

⁹ Istituto Nazionale di Fisica Nucleare, Sezione di Padova, I-35131 Padova, Italy

¹⁰ Dipartimento di Fisica "G. Galilei," Università di Padova, I-35131 Padova, Italy

¹¹ CNRS, IRAP, F-31028 Toulouse Cedex 4, France

¹² GAHEC, Université de Toulouse, UPS-OMP, IRAP, Toulouse, France

¹³ Dipartimento di Fisica, "M. Merlin" dell'Università e del Politecnico di Bari, I-70126 Bari, Italy

¹⁴ Istituto Nazionale di Fisica Nucleare, Sezione di Bari, I-70126 Bari, Italy

¹⁵ Laboratoire Leprince-Ringuet, École polytechnique, CNRS/IN2P3, Palaiseau, France

¹⁶ Institut de Ciències de l'Espai (IEEE-CSIC), Campus UAB, E-08193 Barcelona, Spain

¹⁷ INFN-Istituto di Astrofisica Spaziale e Fisica Cosmica, I-20133 Milano, Italy

¹⁸ Center for Earth Observing and Space Research, College of Science, George Mason University, Fairfax, VA 22030, USA

¹⁹ Agenzia Spaziale Italiana (ASI) Science Data Center, I-00044 Frascati (Roma), Italy

²⁰ Laboratoire Univers et Particules de Montpellier, Université Montpellier 2, CNRS/IN2P3, Montpellier, France

²¹ Department of Physics, Stockholm University, AlbaNova, SE-106 91 Stockholm, Sweden

²² The Oskar Klein Centre for Cosmoparticle Physics, AlbaNova, SE-106 91 Stockholm, Sweden

²³ IASF Palermo, I-90146 Palermo, Italy

²⁴ INFN-Istituto di Astrofisica Spaziale e Fisica Cosmica, I-00133 Roma, Italy

²⁵ Dipartimento di Fisica, Università di Udine and Istituto Nazionale di Fisica Nucleare, Sezione di Trieste, Gruppo Collegato di Udine, I-33100 Udine, Italy

²⁶ Space Science Division, Naval Research Laboratory, Washington, DC 20375-5352, USA

²⁷ NASA Goddard Space Flight Center, Greenbelt, MD 20771, USA

²⁸ Department of Physical Sciences, Hiroshima University, Higashi-Hiroshima, Hiroshima 739-8526, Japan

²⁹ Department of Physics and Astrophysics, Nagoya University, Chikusa-ku Nagoya 464-8602, Japan

³⁰ INFN-Istituto di Radioastronomia, I-40129 Bologna, Italy

³¹ Center for Space Plasma and Aeronomic Research (CSPAR), University of Alabama in Huntsville, Huntsville, AL 35899, USA

³² Department of Astronomy, Graduate School of Science, Kyoto University, Sakyo-ku, Kyoto 606-8502, Japan

³³ Centre d'Études Nucléaires de Bordeaux Gradignan, IN2P3/CNRS, Université Bordeaux 1, BP120, F-33175 Gradignan Cedex, France

³⁴ Department of Physics, Center for Cosmology and Astro-Particle Physics, The Ohio State University, Columbus, OH 43210, USA

³⁵ Department of Physics, Royal Institute of Technology (KTH), AlbaNova, SE-106 91 Stockholm, Sweden

³⁶ Science Institute, University of Iceland, IS-107 Reykjavik, Iceland

³⁷ College of Science, Ibaraki University, 2-1-1, Bunkyo, Mito 310-8512, Japan

³⁸ Research Institute for Science and Engineering, Waseda University, 3-4-1, Okubo, Shinjuku, Tokyo 169-8555, Japan

³⁹ Department of Astronomy, Stockholm University, SE-106 91 Stockholm, Sweden

⁴⁰ Yukawa Institute for Theoretical Physics, Kyoto University, Kitashirakawa Oiwake-cho, Sakyo-ku, Kyoto 606-8502, Japan

⁴¹ Department of Physics, Graduate School of Science, University of Tokyo, 7-3-1 Hongo, Bunkyo-ku, Tokyo 113-0033, Japan

⁴² Center for Research and Exploration in Space Science and Technology (CRESST) and NASA Goddard Space Flight Center, Greenbelt, MD 20771, USA

⁴³ Department of Physics and Department of Astronomy, University of Maryland, College Park, MD 20742, USA

- ⁴⁴ Istituto Nazionale di Fisica Nucleare, Sezione di Roma “Tor Vergata,” I-00133 Roma, Italy
⁴⁵ Department of Physics, Boise State University, Boise, ID 83725, USA
⁴⁶ Institute of Space and Astronautical Science, JAXA, 3-1-1 Yoshinodai, Chuo-ku, Sagami-hara, Kanagawa 252-5210, Japan
⁴⁷ Hiroshima Astrophysical Science Center, Hiroshima University, Higashi-Hiroshima, Hiroshima 739-8526, Japan
⁴⁸ Department of Physics and Astronomy, University of Denver, Denver, CO 80208, USA
⁴⁹ Max-Planck-Institut für Physik, D-80805 München, Germany
⁵⁰ Santa Cruz Institute for Particle Physics, Department of Physics and Department of Astronomy and Astrophysics, University of California at Santa Cruz, Santa Cruz, CA 95064, USA
⁵¹ Institut für Astro-und Teilchenphysik and Institut für Theoretische Physik, Leopold-Franzens-Universität Innsbruck, A-6020 Innsbruck, Austria
⁵² Department of Physics, University of Washington, Seattle, WA 98195-1560, USA
⁵³ NYCB Real-Time Computing Inc., Lattingtown, NY 11560-1025, USA
⁵⁴ Max-Planck Institut für extraterrestrische Physik, D-85748 Garching, Germany
⁵⁵ Institut für Theoretische Physik and Astrophysik, Universität Würzburg, D-97074 Würzburg, Germany
⁵⁶ Institució Catalana de Recerca i Estudis Avançats (ICREA), Barcelona, Spain
⁵⁷ Consorzio Interuniversitario per la Fisica Spaziale (CIFS), I-10133 Torino, Italy
⁵⁸ INTEGRAL Science Data Centre, CH-1290 Versoix, Switzerland
⁵⁹ Dipartimento di Fisica, Università di Roma “Tor Vergata,” I-00133 Roma, Italy
Received 2012 April 22; accepted 2012 June 25; published 2012 August 8

ABSTRACT

We report on the gamma-ray observations of giant molecular clouds Orion A and B with the Large Area Telescope (LAT) on board the *Fermi Gamma-ray Space Telescope*. The gamma-ray emission in the energy band between ~ 100 MeV and ~ 100 GeV is predicted to trace the gas mass distribution in the clouds through nuclear interactions between the Galactic cosmic rays (CRs) and interstellar gas. The gamma-ray production cross-section for the nuclear interaction is known to $\sim 10\%$ precision which makes the LAT a powerful tool to measure the gas mass column density distribution of molecular clouds for a known CR intensity. We present here such distributions for Orion A and B, and correlate them with those of the velocity-integrated CO intensity (W_{CO}) at a $1^\circ \times 1^\circ$ pixel level. The correlation is found to be linear over a W_{CO} range of ~ 10 -fold when divided in three regions, suggesting penetration of nuclear CRs to most of the cloud volumes. The W_{CO} -to-mass conversion factor, X_{CO} , is found to be $\sim 2.3 \times 10^{20} \text{ cm}^{-2} (\text{K km s}^{-1})^{-1}$ for the high-longitude part of Orion A ($l > 212^\circ$), ~ 1.7 times higher than $\sim 1.3 \times 10^{20}$ found for the rest of Orion A and B. We interpret the apparent high X_{CO} in the high-longitude region of Orion A in the light of recent works proposing a nonlinear relation between H_2 and CO densities in the diffuse molecular gas. W_{CO} decreases faster than the H_2 column density in the region making the gas “darker” to W_{CO} .

Key words: gamma rays; ISM – ISM: clouds – ISM: general – ISM: individual objects (Orion A and Orion B)

Online-only material: color figures

1. INTRODUCTION

The Orion A and B clouds are the archetypes of local giant molecular clouds where interstellar gas condenses and stars are formed (e.g., Bergin & Tafalla 2007; Bally 2008, and references therein). The clouds have been studied in various wave bands including millimeter observations of the transition lines between CO rotational states, especially from $J = 1$ to $J = 0$ (e.g., Sanders et al. 1984; Maddalena et al. 1986; Dame et al. 1987, 2001; Wilson et al. 2005; Y. Fukui et al. 2011, private communication), infrared emission (e.g., Beichman et al. 1988), attenuation of star light (e.g., Dobashi et al. 2005), and near-infrared extinction (Rowles & Froebrich 2009; Froebrich & Rowles 2010; Dobashi 2011). The two clouds are prime targets for the Large Area Telescope (LAT), on board the *Fermi Gamma-ray Space Telescope* (*Fermi*), in the research of molecular clouds and cosmic-ray (CR) interaction because they lie isolated from the Galactic plane and there are no intense gamma-ray point source overlaps with the clouds (Abdo et al. 2009c; Abdo et al. 2010b).

Gamma rays from the Orion–Monoceros region were first detected by COS-B in the energy range between 100 MeV and 5 GeV (Caraveo et al. 1980; Bloemen et al. 1984). EGRET

detected gamma rays in the range between 100 MeV and ~ 10 GeV (Digel et al. 1995, 1999). In these studies, the gamma-ray intensity distribution in a region including Orion A, B, and Monoceros R2 was fitted with three independent contributions, one proportional to the atomic hydrogen (H I) column density, another proportional to the CO line intensity (W_{CO}),⁶³ and the last, a presumed isotropic distribution. Under the assumptions that W_{CO} traces the H_2 column density, the CR spectrum does not change in the region and H I spin temperature (T_S) is constant, the ratio X_{CO} was determined,⁶⁴ from the ratio of the gamma-ray intensities associated with the H I and CO distributions, to be $X_{\text{CO}} = (2.6 \pm 1.2) \times 10^{20} \text{ cm}^{-2} (\text{K km s}^{-1})^{-1}$ (Bloemen et al. 1984) and $X_{\text{CO}} = (1.35 \pm 0.15) \times 10^{20} \text{ cm}^{-2} (\text{K km s}^{-1})^{-1}$ (Digel et al. 1999). The ratio was not separately measured for the three clouds, Orion A, B, and Monoceros R2, due to the limited statistics and spatial resolution of the instruments.

⁶³ We define W_{CO} as the velocity-integrated intensity of the transition line between $J = 1$ to $J = 0$ in $^{12}\text{C}^{16}\text{O}$.

⁶⁴ Our X_{CO} is a factor converting W_{CO} to mass column density measured in units of the proton mass in cloud concentrations predominantly consisting of H_2 . In some literature, X_{CO} is used as the factor converting W_{CO} to H_2 column density. Where W_{CO} traces H_2 accurately and the chemical state of hydrogen is predominantly in H_2 , the two definitions are expected to agree. The helium and heavier atoms are assumed to be mixed uniformly in the interstellar gas with the solar abundance. We warn readers that comparison of X_{CO} values calculated on different CO surveys and gamma-ray observations are not straightforward due to differences in their calibration procedure (e.g., see Bronfman et al. 1988, for the CO calibration factor) as well as in the assumptions on the CR composition and the associated cross-sections.

⁶⁰ Resident at Naval Research Laboratory, Washington, DC 20375, USA.

⁶¹ Royal Swedish Academy of Sciences Research Fellow, funded by a grant from the K. A. Wallenberg Foundation.

⁶² NASA Postdoctoral Program Fellow, USA.

We note that Strong et al. (1988) determined X_{CO} on the diffuse Galactic gamma rays observed by COS-B to be $X_{\text{CO}} = (2.3 \pm 0.3) \times 10^{20} \text{ cm}^{-2} (\text{K km s}^{-1})^{-1}$ and Dame et al. (2001), by comparing smoothed infrared intensity and W_{CO} distributions across the Galaxy, determined it to be $X_{\text{CO}} = (1.8 \pm 0.3) \times 10^{20} \text{ cm}^{-2} (\text{K km s}^{-1})^{-1}$.

Since the publications on the EGRET data (Digel et al. 1995, 1999), much progress has been made in studies on Orion A and B: new observational data became available (e.g., Dame et al. 2001; Lombardi & Alves 2001; Wilson et al. 2005; Kalberla et al. 2005; Dobashi et al. 2005; Rowles & Froebrich 2009; Froebrich & Rowles 2010; Dobashi 2011); study of the molecular clouds was renewed (e.g., Wilson et al. 2005; Bally 2008); a new modeling of the Galactic diffuse gamma-ray emission was proposed incorporating large-scale CR propagation (Strong & Moskalenko 1998; Strong et al. 2000); theoretical calculations of collisional CO rotational-level excitation were revisited (Mengel et al. 2001; Flower 2001; Cecchi-Pestellini et al. 2002; Balakrishnan et al. 2002; Wernli et al. 2006; Shepler et al. 2007; see also Kalberla et al. 2005; Liszt 2006, 2007); and the distance to the Orion Nebula in the Orion A cloud was measured accurately (Sandstrom et al. 2007; Menten et al. 2007; Hirota et al. 2007; Kim et al. 2008).

The *Fermi Gamma-ray Space Telescope* mission, launched on 2008 June 11, has been surveying the sky with the LAT since 2008 August. Its wide field of view, large effective area, improved spatial resolution, and broad energy coverage provide much higher sensitivity relative to its predecessor EGRET (Atwood et al. 2009; Abdo et al. 2009a).

Studies based on EGRET observations have established that gamma rays from Galactic molecular clouds are dominated by neutral pion decays (which we refer to as the “pionic gamma rays” or “pionic emission”) in the energy band between 0.2 GeV and 10 GeV (Bertsch et al. 1993; Digel et al. 1995, 1999). Orion A and B are located far (~ 8.8 kpc) from the Galactic center⁶⁵ and are displaced from the Galactic plane by ~ 140 pc. The two clouds are only ~ 400 pc away from the solar system where spectra of CR species up to the sub-TeV domain are predicted to be similar to those measured directly at the Earth after correction for the solar modulation.

We can now analyze Orion A and B through the high-energy gamma rays detected by the *Fermi*-LAT in the light of the recent developments and study the relation between W_{CO} and mass column density (or X_{CO}) in various parts of the Galaxy and obtain the total mass of the clouds.⁶⁶ The improved spatial resolution and higher gamma-ray statistics provided by the *Fermi*-LAT allow us to determine the relation on angular scales of $1 \times 1 \text{ deg}^2$ (pixels), without being directly affected by the thermodynamical, chemical, or radiation environment inside the Orion clouds, albeit within the limited angular resolution of the *Fermi*-LAT and uncertainties due to any unresolved weak sources and CR flux variation. The results can be used conversely to study various environmental effects on X_{CO} in the translucent parts of clouds where most gas in Orion A and B resides and where the X_{CO} factor has not been straightforward to derive (e.g., van Dishoeck & Black 1986; Magnani et al. 1988; Bolatto et al. 1999; Magnani et al. 2003; Bell et al. 2006; Snow

& McCall 2006; Bell et al. 2007; Burgh et al. 2007; Wall 2007; Sheffer et al. 2008).

Theoretical analyses have long suggested that X_{CO} depends on the environment and the $W_{\text{CO}}-N(\text{H}_2)$ relation may be nonlinear (e.g., Kutner & Leung 1985; Dickman et al. 1986; Maloney & Black 1988; Taylor et al. 1993; Bolatto et al. 1999; Magnani et al. 2003; Bell et al. 2007; Burgh et al. 2007). Suggestions have also been made that X_{CO} depends on the relative abundances of CO, C I, and C II (e.g., van Dishoeck & Black 1988; Hollenbach et al. 1991; Kopp et al. 2000). The existence of gas not traced by H I and CO at the interface between the two phases (the “dark gas”) has been discovered (Grenier et al. 2005; Ade et al. 2011). The relation between the fraction of carbon in CO and H₂ density in translucent and diffuse clouds has been updated based on observations and numerical simulations, for example, by Burgh et al. (2010), Wolfire et al. (2010), and Glover et al. (2010). Our results will be interpreted in the light of these recent works. The $W_{\text{CO}}-N(\text{H}_2)$ relation will be characterized including the “dark gas,” and the measured mass column density will be related to the A_V value at which the relation is predicted to become nonlinear.

In this paper, we analyze diffuse gamma rays spatially associated with the molecular clouds⁶⁷ Orion A and B, extract their pionic gamma-ray components, obtain mass distributions, and compare them with those predicted for W_{CO} measured by Y. Fukui et al. (2011, private communication) and Dame et al. (2001). In Section 2, we describe the gamma-ray event selection applied in this analysis. The analysis procedure is described in Section 3 in four subsections: the spatial templates used to extract mass column density associated with multiple emission components are given in Section 3.1, energy-binned spatial fits on the templates are described in Section 3.2, the pionic emission is extracted from the spectra obtained in the spatial fits and X_{CO} is calculated thereon in Section 3.3, and the total H₂ masses of Orion A and B are estimated in Section 3.4. In Section 4, we assess systematic uncertainties in the analyses, check the X_{CO} results with recent infrared excess emission maps by Dobashi (2011), summarize the results, and interpret them in the light of recent studies of the relation between the H₂ and CO fraction in the translucent clouds. The paper is concluded in Section 5.

2. OBSERVATIONS AND DATA

The data used in this analysis were obtained in the nominal all-sky survey mode between 2008 August 4 and 2010 March 11.⁶⁸ We select events classified as *Pass6 Diffuse* class which has a high gamma-ray purity (Atwood et al. 2009). Among the events, we limit the reconstructed zenith angle to be less than 105° to greatly reduce gamma rays coming from the limb of the Earth’s atmosphere. We select the good time intervals of the observations by excluding events that were taken while the instrument rocking angle was larger than 52° . Another cut is made on the reconstructed gamma-ray energy at $E_{\text{min}} = 178 \text{ MeV}$ and $E_{\text{max}} = 100 \text{ GeV}$ to reduce systematic uncertainty of the LAT effective area and residual background events induced by CRs. Gamma rays in a rectangular region of $30^\circ \times 30^\circ$ centered at ($\ell = 210^\circ$, $b = -20^\circ$) are then selected

⁶⁵ We assume the distance between the Sun and the Galactic center to be 8.5 kpc and the Galactic rotation velocity near the Sun to be 220 km s^{-1} .

⁶⁶ The mass of Orion A and B is distributed mostly in the column density range corresponding to a “translucent” cloud whose line-of-sight visual attenuation (A_V) is typically between 1 and 5 mag and has $n(\text{H}_2)$ typically between 100 and 2000 cm^{-3} (e.g., van Dishoeck & Black 1988).

⁶⁷ By molecular clouds we mean spatially identified clouds without distinguishing the small admixture of atomic and ionized hydrogens therein.

⁶⁸ Mission Elapsed Time 239,557,413 s through 290,000,000 s where zero is set at 00:00 UTC on 2001 January 1. During the period, the LAT was operated in the survey mode with the rocking angle 35° (2008 August 4 to 2009 July 9), 39° (2009 July 9 to 2009 September 3), and 50° (2009 September 3 to 2010 March 11).

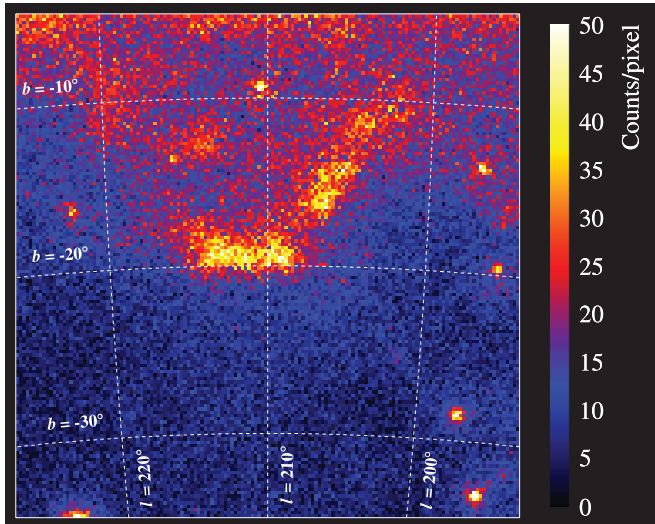


Figure 1. Gamma-ray count distribution in the Orion region in the energy band between 178 MeV and 100 GeV in the Hammer–Aitoff projection on the Galactic coordinates. The pixel size is $0.2 \times 0.2 \text{ deg}^2$.

(A color version of this figure is available in the online journal.)

for later analyses. We refer to the region as the region of interest (ROI) and the set of events as the data set.

The data set consists of 1,132,436 events of which 901,929 are between 178 MeV and 1 GeV, 224,753 between 1 GeV and 10 GeV, and 5754 between 10 GeV and 100 GeV. They are binned in 150×150 equal-area pixels (Hammer–Aitoff projection) in Galactic coordinates with 0.2 gridding on their reconstructed arrival directions, and in 22 logarithmic bins between $E_{\min} = 178 \text{ MeV}$ and $E_{\max} = 100 \text{ GeV}$ on their reconstructed energies.

The map of counts integrated over the energy range of the data set is shown in Figure 1. We can visually identify Orion A and B near the center of the region and the outer Galactic plane in the upper part. We note that Monoceros R2 is also visible between Orion A/B and the outer Galactic plane.

3. ANALYSES

The analyses presented here begin by finding the relationship between the spatial distributions of gamma rays and W_{CO} , the most widely used proxy of H_2 , in the Orion clouds and by studying the proportionality between the two and its spatial dependence within the Orion clouds. The analyses proceed in three steps.

In the first step, the spatial distribution of the “background” gamma rays, i.e., the gamma rays not associated with the H_2 clouds, is determined by using spatial distribution templates, for the H I gas, for the inverse Compton (IC) scattering component, for the point sources, and for a presumed isotropic component (Section 3.1). We then fit, in Section 3.2, the gamma-ray spatial distribution in each of the 22 energy bins as a sum of the “background” distribution and a distribution tentatively associated with the H_2 gas (H_2 template). The “background” is subtracted from the measured gamma-ray intensity distribution and the remainder is defined as the gamma-ray intensity distribution associated with the H_2 gas with which W_{CO} is correlated pixel by pixel. We note that the gamma-ray intensity measures the mass column density in the H_2 gas for a known CR spectrum. We repeat the fit with two alternative H_2 templates.

In the second step (Sections 3.3 and 3.4), the energy-binned gamma-ray emissivity for the H_2 gas (B_i in Equation (1)) is assembled as the gamma-ray spectrum for each of the three H_2 templates. The spectrum is then fitted as a sum of the gamma rays produced in the pionic and bremsstrahlung processes.

In the third step, the gamma-ray intensity distribution associated with the pionic emission is converted to the mass column density. The W_{CO} –mass conversion factor (X_{CO}) is calculated via two methods, one by comparing the gamma-ray counts associated with the H I gas and with the H_2 gas (the $\text{H}_2/\text{H I}$ method) and the other by dividing the gamma-ray counts of the pionic emission by the number of pionic gamma rays expected per unit gas mass (the pionic method). In the first method, we assume the CR spectrum is uniform in the local H I region within Galactocentric radius of 8–10 kpc (see Section 3.1.1) and in the Orion clouds. In the latter method, we assume the CR spectrum including its absolute flux is known in the Orion clouds. We validate these assumptions using GALPROP.

We use GALPROP (Strong & Moskalenko 1998; Strong et al. 2000) with the parameter set labeled as GALDEF 54_77Xvarh7S. This parameter set is known to reproduce reasonably well the Galactic diffuse gamma-ray emission observed with the LAT (Abdo et al. 2009e).⁶⁹ We refer to the results obtained by running GALPROP with this parameter set as the GALPROP results in this paper.

3.1. Spatial Distribution Templates

Initially, we assume the gamma-ray emission from the ROI to be made of four “background” components and one “signal” H_2 component, each emitting gamma rays with a characteristic spatial distribution. The four “background” components are spatially associated with the diffuse H I gas, the IC scattering by electrons⁷⁰ off interstellar radiation fields, the point sources, and the sum of extragalactic diffuse emission (including unresolved sources) and backgrounds induced by CRs in the instrument. We assume the last sum to be isotropic and refer to it as the isotropic component. We ignore the contribution from ionized hydrogen gas (H II) because its density is low when averaged in $1 \times 1 \text{ deg}^2$ pixels ($<0.5 \text{ cm}^{-3}$) and its total mass is negligible in the ROI (Gordon 1969; O’Dell 2001).

All spatial components except for the IC component are assumed to have, individually, an energy-independent underlying spatial distribution in Galactic coordinates (l, b). Another important underlying assumption is that the nuclear CR spectrum is uniform over the ROI. We make spatial templates for the 22 energy bins by convolving the spatial distributions with the energy-dependent point-spread function (PSF) and exposure for the individual energy bins. Hence, the spatial templates are energy dependent. In Section 3.3, we will show that the spectra of the gamma-ray emissions associated with the H I and H_2 gas consist of the pionic and bremsstrahlung components.

The gamma-ray intensity $I_{\gamma,i}(l, b)$ for the i th energy bin is interpreted as the sum of the five contributions, each being the product of the normalization factor for the i th energy bin and the spatial template.

$$I_{\gamma,i}(l, b) = A_i N(\text{H I})(l, b) + B_i N(\text{H}_2)(l, b) + \text{IC}_i(l, b) + \sum_j (C_{ij} \delta_{l_j, b_j}) + D_i. \quad (1)$$

⁶⁹ A detailed description of GALDEF files can be found at <http://galprop.stanford.edu>

⁷⁰ We refer to electrons as a sum of e^+ and e^- .

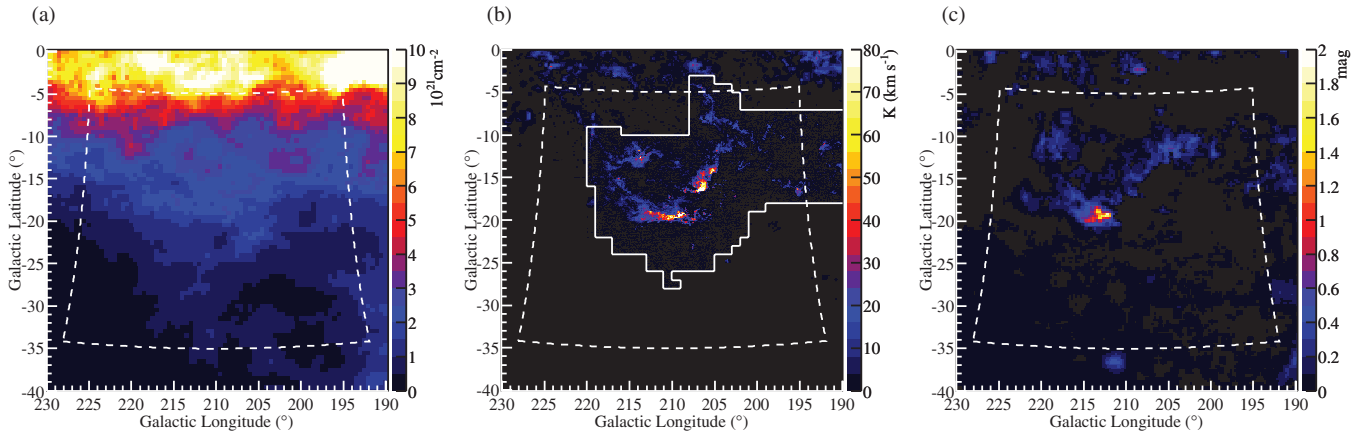


Figure 2. (a) $N(\text{H I})$ template summed over the line-of-sight velocity. The pixel size is $0:5 \times 0:5$. The dashed lines show the boundary of the ROI. (b) W_{CO} template used in H_2 -template-1 and H_2 -template-2. We used NANTEN data (Y. Fukui et al. 2011, private communication) in the area bounded by the solid lines and those by Dame et al. (2001) elsewhere. Pixel resolution is $0:125 \times 0:125$. (c) $E(B - V)_{\text{res}}$ template used in H_2 -template-3. Pixel resolution is $0:5 \times 0:5$.

(A color version of this figure is available in the online journal.)

The normalization factors are A_i for the H I gas, B_i for the component associated with clouds consisting predominantly of H_2 , IC_i for the IC component, $C_{ij}\delta_{l_j, b_j}$ for the j th point source at (l_j, b_j) , and D_i for the isotropic component which is assumed not to depend on (l, b) . The normalization factors are determined independently for the 22 energy bins. We note that IC_i are fixed at the values given by GALPROP, because the spatial distribution is highly correlated with the isotropic component, and the IC component is sub-dominant in the ROI.

Later in Section 3.2, we will explore three templates for H_2 , two based on W_{CO} and one on W_{CO} plus the “dark gas” proposed by Grenier et al. (2005).

3.1.1. Diffuse H I Gas Template

Atomic hydrogen gas (H I) is broadly distributed in the Galaxy with a total mass exceeding that of molecular hydrogen (H_2 ; e.g., Ferrière 2001; Snow & McCall 2006). In the outer Galaxy where the Orion clouds are located, the mass column density of H I is lower than that of H_2 at the Orion clouds (Kalberla et al. 2010, 2005).

We used the Leiden/Argentine/Bonn (LAB) survey data (Kalberla et al. 2005) corrected for optical thickness by adopting a constant spin temperature (T_S) of 125 K as the H I gas spatial distribution template (see Figure 2(a)). The LAB intensity distribution is divided into five annuli centered at the Galactic center as has been done in other *Fermi* diffuse emission analyses (Abdo et al. 2010c). Their inner and outer Galactocentric radii (R) are 8–10, 10–11.5, 11.5–16.5, 16.5–19, and 19–50 kpc. The line-of-sight velocity distribution of the H I gas in the Orion region overlaps that of the CO gas associated with the Orion clouds and that of the local H I annulus ($R = 8$ –10 kpc) quite well.

Gamma-ray contributions from all the H I annuli overlapping our ROI have been included in the analyses. In the fitting, the CR intensity is treated independently at each annulus. The contributions from annuli other than the local one ($R = 8$ –10 kpc) are through the periphery of the LAT PSF and less than $\sim 5\%$ in gamma-ray counts. Hence, our analyses are insensitive to variation in the CR intensity and/or spectrum among the neighboring annuli.

The spin temperature of H I gas, T_S , is not well constrained in the region nor known to be uniform over the ROI: its quoted value in the literature ranges between ~ 90 K and ~ 400 K

(e.g., Mohan et al. 2004a, 2004b). We estimate, later in this paper, the contribution to the overall systematic error from this uncertainty by repeating the analysis for $T_S = 250$ K and 90 K. No significant concentration of cold H I is known around Orion A and B at large scale ($> 1 \times 1 \text{ deg}^2$; Kalberla et al. 2010). An exploratory study of cold H I mixed in selected H_2 cloud cores has found the mean H I fraction to be less than 0.5% (Krčo et al. 2008). So we can safely ignore such a mixture in the analysis.

Gamma rays are produced in the H I gas through the pionic and bremsstrahlung processes with intensities proportional to the CR nuclear and electron spectra in the gas, respectively.

3.1.2. Molecular Cloud Template

We try three H_2 templates to represent the H_2 spatial distribution in the ROI. In making the templates, we assume that the H_2 column density is proportional to W_{CO} measured by two CO ($J = 1 \rightarrow 0$) surveys, one from NANTEN (Y. Fukui et al. 2011, private communication) covering the areas around the Orion clouds with effective resolution of $4'$ and the other being the Galactic survey by Dame et al. (2001) covering the ROI with angular resolution of $8:7$. The spatial distributions indicated by the two surveys are mutually consistent at the angular scale of the LAT PSF except for the overall normalization.

The first H_2 template, H_2 -template-1, is made by combining the two surveys and accounting for their relative intensity scales (Figure 2(b)): NANTEN W_{CO} for the area defined by the solid white line and that by Dame et al. (2001) for the rest of the region. We refer to the three regions defined by dashed lines in Figure 3(b) as “the three Orion regions” hereafter.⁷¹ We scale the NANTEN data by the factor $1/1.11$ to adjust the intensities to a common scale with Dame et al. (2001) because the survey by Dame et al. (2001) has been widely used in gamma-ray analyses.

We first start the analyses by setting one common B_i factor for W_{CO} in the ROI (H_2 -template-1), or equivalently, one common X_{CO} for the entire ROI. In the second H_2 template, H_2 -template-2, the W_{CO} distribution is divided into four regions (the three Orion regions and the rest of the ROI) and allow B_i , or equivalently X_{CO} , to be different in each region. We add a

⁷¹ The boundaries are Orion A Region I ($217^\circ > l > 212^\circ, -23^\circ < b < -16^\circ$), Orion A Region II ($212^\circ > l > 205^\circ, -23^\circ < b < -16^\circ$, excluding the overlap with Orion B), and Orion B ($209^\circ > l > 203^\circ, -18^\circ < b < -13^\circ$).

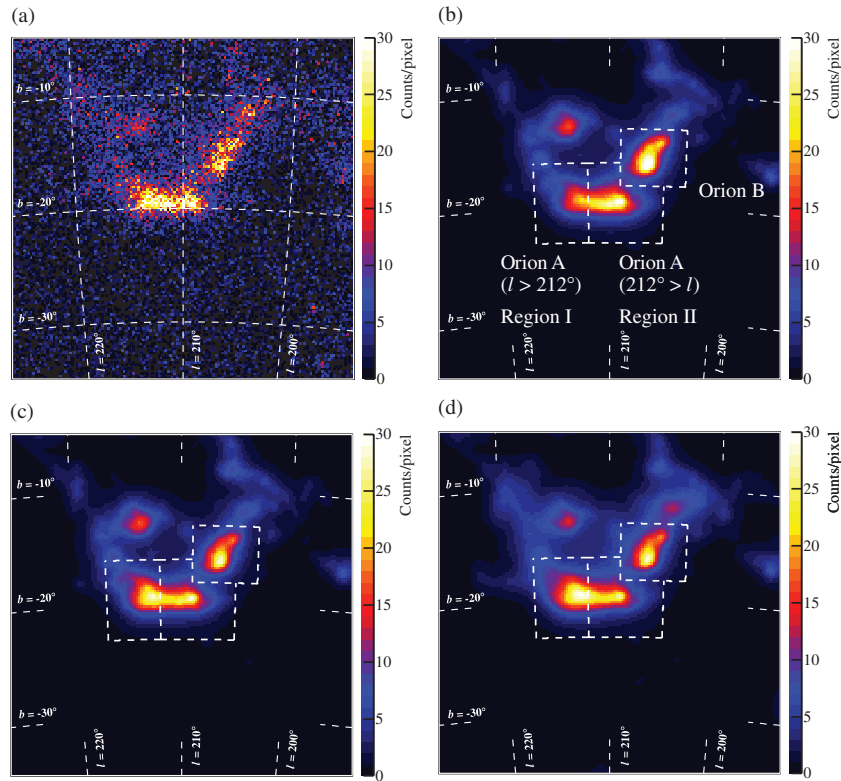


Figure 3. (a) Gamma-ray count distribution in the ROI after subtracting the fitted “background” that is the sum of the H I, IC, point-source, and isotropic components. (b) The fitted model map obtained by assuming one common X_{CO} for the ROI (H₂-template-1). Dashed lines define the boundaries of the three Orion regions, Orion A Region I, Region II, and Orion B. (c) Same as (b) but obtained by assuming four different X_{CO} for Orion A Region I, Region II, Orion B, and elsewhere (H₂-template-2). (d) Same as (b) but obtained by adding $E(B - V)_{\text{res}}$ to H₂-template-1 (H₂-template-3).

(A color version of this figure is available in the online journal.)

“dark-gas” template (Grenier et al. 2005) to H₂-template-1 to make the third H₂ template, H₂-template-3 (Figures 2(a) and (c)). The normalization is set free for the two templates.

These spatial templates are described further in the subsections to follow.

3.1.3. Inverse Compton Template

The IC component is known to be minor around the Orion clouds. We use the IC spectrum and spatial distribution given by GALPROP where the interstellar photon fields are taken from Porter et al. (2008). The typical Galactic-scale IC intensity in the region is ~ 5 times smaller than the isotropic component described later, and their spatial and spectral distributions are similar in this region. Possible local enhancement is the IC emission around the Orion Nebula (M42) where strong ultraviolet emission (e.g., Murthy et al. 2005) and moderate infrared emission (e.g., Prisinzano et al. 2008) exist. According to our calculation, such IC emissions are not detectable with the current LAT sensitivity (Orlando & Strong 2008).

3.1.4. Point Sources in the Orion Region

More than 1400 point sources are reported in the First *Fermi*-LAT Catalog (Abdo et al. 2010b). Among them, 30 point sources are in our ROI, $(l, b) = (210^\circ \pm 15^\circ, -20^\circ \pm 15^\circ)$. There are an additional 29 sources within 5° of the ROI. In the likelihood fit to be discussed later, the normalization is set free, energy bin by energy bin, for 25 high-confidence sources in the ROI; the indexes and normalizations are fixed to the values given in the First *Fermi*-LAT Catalog (Abdo et al. 2010b)

for those outside of the region. There are five low-confidence sources (or candidates) overlapping with the clouds: they are⁷² 1FGL J0540.4–0737c, J0536.2–0607c, J0534.7–0531c, J0541.9–0204c, and J0547.0+0020c. Their fluxes are all low and labeled as “c” in the catalog, meaning either their flux estimates are uncertain, or they can be artifacts resulting from incorrect modeling of the Galactic diffuse emission. We fit the spatial templates and analyze the spectra in the three Orion regions with and without them. The results we quote will be for the analyses without them: we include their possible contribution in the systematic error.

3.1.5. Isotropic Component

In the present analyses, the extragalactic emission and residual CR background in the data are not separated but treated as a single isotropic component (Abdo et al. 2009b, 2010c; Ackermann et al. 2010; Abdo et al. 2010a). The total flux of the component at 1 GeV is $\sim 25\%$ of that associated with H₂ when averaged over the three Orion regions (subtending ~ 30 msr) defined around Orion A and B (see Figure 3(b)).

The residual background in the *Pass6 Diffuse* class consists of CR-induced events misclassified as gamma rays and CRs that converted in the passive material just outside of the LAT without leaving a signal in the anti-coincidence detector (Atwood et al. 2009). When averaged over many orbits of observations, the residual background can be approximated as isotropic.

⁷² No new sources have been added in this region in the Second *Fermi* LAT Catalog (Nolan et al. 2012).

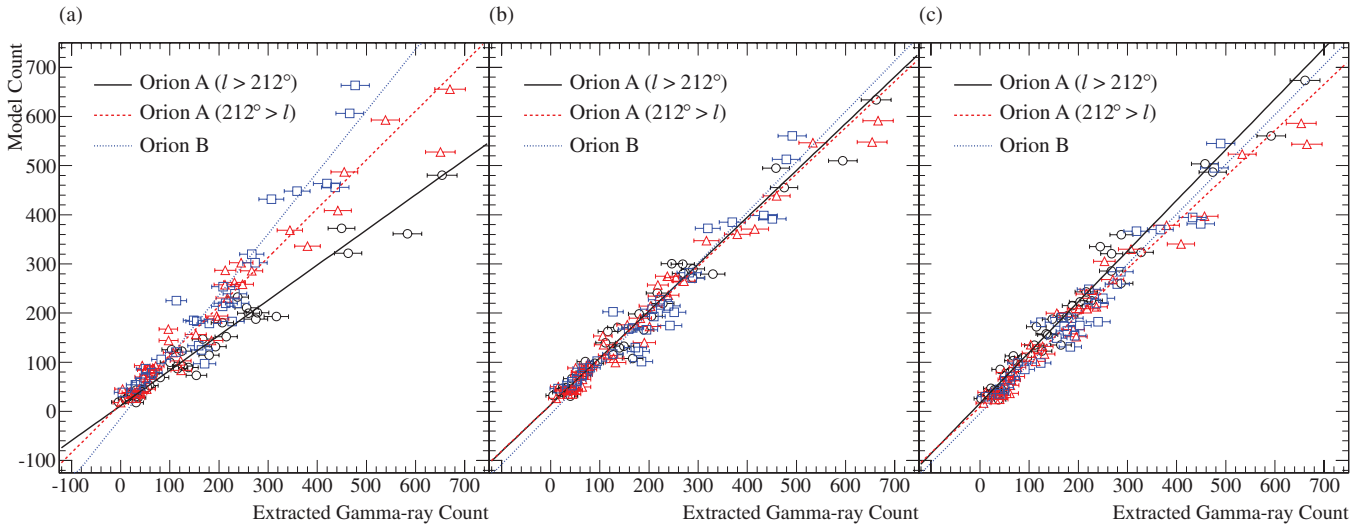


Figure 4. (a) Correlation between the gamma-ray count distribution shown in Figure 3(a) (the horizontal axis) and that fitted with H_2 -template-1 in Figure 3(b) (the vertical axis) for all pixels in the three Orion regions. Points represent pixels in Orion A Region I (black circles), Region II (red triangle), and Orion B (blue squares) with fitted lines black, red, and blue, respectively. Error bars represent statistical errors in counts in pixels. Same after replacing the vertical axis for that fitted with H_2 -template-2 (b) and for that fitted with H_2 -template-3 (the sum of W_{CO} and $E(B - V)_{res}$ components) (c).

(A color version of this figure is available in the online journal.)

3.2. Fit to the Spatial Distribution

All spatial templates described in the previous subsection were convolved with the LAT exposure and PSF. The spatial fit is made using the binned likelihood program *gtlike* included in the *Fermi* ScienceTools⁷³ and the four normalizations (A_i , B_i , C_{ij} , and D_j) in Equation (1) are determined independently for the 22 energy bins. We note again that IC_i are fixed at the values given by GALPROP. Each H I annulus has a separate A_i . We report only A_i for the local annulus as others are not determined well because they lie mostly outside of our ROI.

Our scientific interest is to study the contributions from the gas concentrations identified as Orion A and B, which are believed to be predominantly H_2 . We consider, hence, the sum of the H I, IC, point-source, and isotropic components as the “background” which is determined by fitting the observed gamma-ray distribution for each of the 22 energy bins. In the fits, we assume that H_2 -template-1, or the W_{CO} distribution, represents approximately the H_2 distribution. The gamma-ray distribution associated with the H_2 gas can be extracted less dependently on yet-unknown H_2 - W_{CO} relation by subtracting the “background” from the observed gamma-ray distribution.

We define two improved H_2 templates, H_2 -template-2 and 3 after the initial analysis on H_2 -template-1. The spatial distribution is not proportional to W_{CO} for the two improved templates and hence the “background” is different for each H_2 template by a small amount. The difference is however negligible.

3.2.1. Spatial Fit with W_{CO} of One X_{CO} : H_2 -template-1

We use H_2 -template-1 as an approximation for the H_2 gas distribution and fit Equation (1) to determine the “background.” The energy-summed gamma-ray distribution after subtracting the “background” is shown in Figure 3(a) and that of the W_{CO} -based model, or the product of ΣB_i in Equation (1) and H_2 -template-1, is given in Figure 3(b). The two count distributions are correlated pixel by pixel ($1 \times 1 \text{ deg}^2$) in the three

Orion regions in Figure 4(a). We expect a good linear correlation between the two if W_{CO} is a good tracer of H_2 .

We note first that the correlation is fairly linear and gives a correlation coefficient⁷⁴ of 0.93. We then note that the correlation significantly improves if we separate the Orion clouds into the three Orion regions, Orion A Region I (black solid line) and II (red dashed line), and Orion B (blue dotted line). The correlation coefficients for the three Orion regions are 0.98, 0.96, and 0.98, and the best-fit slopes are 0.72, 0.99, and 1.25, respectively.

The large difference ($\sim 40\%$ – 60%) in the best-fit slope suggests that the mass column density in Orion A and B cannot be simply derived using the same value of X_{CO} . We find more gamma rays in Orion A Region I per W_{CO} than in Orion A Region II and Orion B, suggesting X_{CO} is different in the three Orion regions, or that some fraction of the H_2 gas is not traced by W_{CO} provided a uniform CR density. We explore these two possibilities by redefining the H_2 template.

3.2.2. Spatial Fit with W_{CO} of Four Different X_{CO} Values: H_2 -template-2

Based on the relation found between the spatial distributions of the gamma-ray intensity associated with the H_2 gas and the W_{CO} -based model (H_2 -template-1), we make a second template, H_2 -template-2, that will delineate the H_2 column density more faithfully. In the template, we divide the ROI into four regions, the three Orion regions and the rest of the ROI, and allow B_i to be different in each region, or introduce four B_i .

The fitted results for A_i (H I) and B_i (H_2 -template-2) in Equation (1) are listed in Table 1 after combining the highest 10 energy bins into three bins. The gamma-ray count map is shown in Figure 3(c) is the sum of the four B_i multiplied with the corresponding components of H_2 -template-2. We note that the three Orion regions mix to some degree through the *Fermi* PSF. The correlation between the gamma-ray distribution associated with H_2 and the H_2 template improved as shown in

⁷³ We use ScienceTools version v9r16p0 with *P6_V3_DIFFUSE* instrument response functions.

⁷⁴ The correlation coefficient is defined as $\Sigma(x - \bar{x})(y - \bar{y}) / \sqrt{\Sigma(x - \bar{x})^2 \Sigma(y - \bar{y})^2}$.

Table 1
Gamma-Ray Emissivity Fitted with H₂-template-2

Energy Range (MeV)	Emissivity per H ^a	Emissivity per W _{CO} ^b		
		Orion Region I	Orion Region II	Orion B
178–237	$(4.81 \pm 0.26) \times 10^{-29}$	$(1.04 \pm 0.08) \times 10^{-28}$	$(5.20 \pm 0.84) \times 10^{-29}$	$(6.17 \pm 0.52) \times 10^{-29}$
237–316	$(3.15 \pm 0.10) \times 10^{-29}$	$(6.36 \pm 0.39) \times 10^{-29}$	$(3.50 \pm 0.37) \times 10^{-29}$	$(3.64 \pm 0.26) \times 10^{-29}$
316–422	$(1.81 \pm 0.04) \times 10^{-29}$	$(3.68 \pm 0.21) \times 10^{-29}$	$(2.16 \pm 0.18) \times 10^{-29}$	$(2.32 \pm 0.13) \times 10^{-29}$
422–562	$(1.05 \pm 0.02) \times 10^{-29}$	$(1.95 \pm 0.11) \times 10^{-29}$	$(1.24 \pm 0.09) \times 10^{-29}$	$(1.17 \pm 0.07) \times 10^{-29}$
562–750	$(5.72 \pm 0.12) \times 10^{-30}$	$(1.29 \pm 0.07) \times 10^{-29}$	$(6.15 \pm 0.46) \times 10^{-30}$	$(6.96 \pm 0.41) \times 10^{-30}$
750–1000	$(3.20 \pm 0.08) \times 10^{-30}$	$(5.97 \pm 0.37) \times 10^{-30}$	$(4.08 \pm 0.27) \times 10^{-30}$	$(3.50 \pm 0.24) \times 10^{-30}$
1000–1334	$(1.69 \pm 0.09) \times 10^{-30}$	$(3.16 \pm 0.23) \times 10^{-30}$	$(2.08 \pm 0.15) \times 10^{-30}$	$(1.70 \pm 0.14) \times 10^{-30}$
1334–1778	$(8.75 \pm 0.30) \times 10^{-31}$	$(1.55 \pm 0.13) \times 10^{-30}$	$(1.06 \pm 0.08) \times 10^{-30}$	$(8.71 \pm 0.80) \times 10^{-31}$
1778–2371	$(4.19 \pm 0.25) \times 10^{-31}$	$(7.49 \pm 0.77) \times 10^{-31}$	$(6.08 \pm 0.53) \times 10^{-31}$	$(4.82 \pm 0.49) \times 10^{-31}$
2371–3162	$(1.83 \pm 0.14) \times 10^{-31}$	$(4.01 \pm 0.47) \times 10^{-31}$	$(2.60 \pm 0.29) \times 10^{-31}$	$(1.92 \pm 0.27) \times 10^{-31}$
3162–4217	$(7.97 \pm 2.72) \times 10^{-32}$	$(2.16 \pm 0.29) \times 10^{-31}$	$(1.23 \pm 0.17) \times 10^{-31}$	$(9.34 \pm 1.56) \times 10^{-32}$
4217–5623	$(4.07 \pm 0.29) \times 10^{-32}$	$(6.98 \pm 1.46) \times 10^{-32}$	$(4.77 \pm 0.95) \times 10^{-32}$	$(4.33 \pm 0.90) \times 10^{-32}$
5623–10000	$(1.19 \pm 0.38) \times 10^{-32}$	$(2.27 \pm 0.47) \times 10^{-32}$	$(1.05 \pm 0.27) \times 10^{-32}$	$(1.10 \pm 0.28) \times 10^{-32}$
10000–23714	$(1.42 \pm 1.01) \times 10^{-33}$	$(2.12 \pm 0.95) \times 10^{-33}$	$(1.48 \pm 0.53) \times 10^{-33}$	$(1.61 \pm 0.59) \times 10^{-33}$
23714–100000	$(4.16 \pm 3.06) \times 10^{-35}$	$(1.07 \pm 0.79) \times 10^{-34}$	$(1.57 \pm 3.34) \times 10^{-34}$	$(1.14 \pm 0.53) \times 10^{-34}$

Notes. Errors are statistical only.

^a MeV⁻¹ s⁻¹ sr⁻¹ per H atom.

^b MeV⁻¹ s⁻¹ sr⁻¹ (2×10^{20} cm⁻² (K km s⁻¹)⁻¹)⁻¹.

Table 2
X_{CO} Obtained on H₂-template-1, 2, and 3

Region	X _{CO} ^a on B/2A	Sys. Error ^b (%)	X _{CO} ^a on Pion	Sys. Error ^c (%)
H ₂ -template-1				
Entire ROI	$1.36 \pm 0.02_{\text{stat}}$	NA	$1.63 \pm 0.02_{\text{stat}}$	NA
H ₂ -template-2				
Orion A Region I	$1.97 \pm 0.05_{\text{stat}}$	+25/–28	$2.34 \pm 0.05_{\text{stat}}$	+30/–32
Orion A Region II	$1.20 \pm 0.03_{\text{stat}}$	+25/–44	$1.43 \pm 0.04_{\text{stat}}$	+30/–49
Orion B	$1.14 \pm 0.03_{\text{stat}}$	+25/–33	$1.35 \pm 0.03_{\text{stat}}$	+30/–38
Elsewhere	$1.43 \pm 0.04_{\text{stat}}$	NA ^c	$1.69 \pm 0.04_{\text{stat}}$	NA ^d
H ₂ -template-3				
Entire ROI	$1.21 \pm 0.02_{\text{stat}}$	+25/–37 ^e	$1.32 \pm 0.02_{\text{stat}}$	+30/–40 ^e

Notes.

^a In unit of 10^{20} cm⁻² (K km s⁻¹)⁻¹.

^b The systematic error is discussed in Section 4.1: it comes from a combination of uncertainties in the H I spin temperature and in the fitting process. The systematic errors which may apply differently to the three Orion regions are +5%/–8%, +5%/–24%, and +5%/–13%, respectively.

^c The systematic error is discussed in Section 4.1. The systematic errors are the same as footnote “b.”

^d We have not attempted to estimate systematic error outside of the Orion regions in this study.

^e The average of the systematic errors estimated for the three Orion regions.

Figure 4(b): the best-fit slopes for Orion A Region I, Region II and Orion B are 0.95, 0.94, and 1.03, respectively, while the correlation factors remain almost the same, 0.98, 0.99, and 0.96, respectively.

The X_{CO} for the four regions can be calculated directly as the ratio of B_i to $2A_i$ (the H₂/H I method) or by extracting the gamma-ray emission in the regions (the pionic method). The results from the former are given in Table 2 together with those from the latter which will be described in Section 3.3.

3.2.3. Spatial Fit with W_{CO} and “Dark Gas”: H₂-template-3

Grenier et al. (2005) found that a significant fraction of local diffuse gamma-ray emission observed by EGRET is not associated with either H I or W_{CO}, but rather with the dust map traced by thermal infrared emission given by Schlegel et al. (1998). The missing gas component is often referred to as the “dark gas.” Other LAT observations have found gamma

rays associated with such “dark gas” (Abdo et al. 2010c; Ackermann et al. 2010). We note recent measurements of attenuation or reddening of background stars have also detected gas concentrations not traced well by W_{CO} (Dobashi et al. 2005; Rowles & Froebrich 2009; Dobashi 2011; Ade et al. 2011).

We make a third template, H₂-template-3, that can bring out the true gas distribution associated with the Orion clouds and enhance our understanding of the W_{CO}-to-H₂ relation by introducing the “dark gas.” The new H₂ template consists of H₂-template-1, or W_{CO}, and a “dark-gas” spatial template with a normalization factor for each.

Our “dark-gas” template has been produced following the prescription given by Grenier et al. (2005) and referred to as $E(B - V)_{\text{res}}$. It is a residual map obtained by subtracting the best-fit linear combination of $N(\text{H I})$ and W_{CO} from the $E(B - V)$ map of Schlegel et al. (1998) as described in Ackermann et al. (2010). Figure 2(c) shows the $E(B - V)_{\text{res}}$ map around our ROI.

Table 3
Gamma-Ray Emissivity Fitted with H₂-template-3

Energy Range (MeV)	Emissivity per H atom ^a	Emissivity per W_{CO} ^b	Emissivity per $E(B - V)_{\text{res}}$ ^c
178–237	$(4.51 \pm 0.08) \times 10^{-29}$	$(5.56 \pm 0.31) \times 10^{-29}$	$(1.00 \pm 0.10) \times 10^{-27}$
237–316	$(2.99 \pm 0.08) \times 10^{-29}$	$(3.39 \pm 0.27) \times 10^{-29}$	$(5.60 \pm 0.83) \times 10^{-28}$
316–422	$(1.68 \pm 0.07) \times 10^{-29}$	$(2.03 \pm 0.11) \times 10^{-29}$	$(3.95 \pm 0.36) \times 10^{-28}$
422–562	$(1.02 \pm 0.08) \times 10^{-29}$	$(1.13 \pm 0.05) \times 10^{-29}$	$(2.07 \pm 0.16) \times 10^{-28}$
562–750	$(5.39 \pm 0.08) \times 10^{-30}$	$(6.51 \pm 0.21) \times 10^{-30}$	$(1.37 \pm 0.09) \times 10^{-28}$
750–1000	$(2.97 \pm 0.09) \times 10^{-30}$	$(3.54 \pm 0.16) \times 10^{-30}$	$(6.57 \pm 0.60) \times 10^{-29}$
1000–1334	$(1.58 \pm 0.05) \times 10^{-30}$	$(1.86 \pm 0.09) \times 10^{-30}$	$(3.57 \pm 0.35) \times 10^{-29}$
1334–1778	$(8.00 \pm 1.02) \times 10^{-31}$	$(9.37 \pm 0.43) \times 10^{-31}$	$(1.86 \pm 0.16) \times 10^{-29}$
1778–2371	$(3.64 \pm 0.25) \times 10^{-31}$	$(5.00 \pm 0.31) \times 10^{-31}$	$(7.45 \pm 1.19) \times 10^{-30}$
2371–3162	$(1.51 \pm 0.14) \times 10^{-31}$	$(2.19 \pm 0.17) \times 10^{-31}$	$(4.82 \pm 0.68) \times 10^{-30}$
3162–4217	$(6.56 \pm 0.89) \times 10^{-32}$	$(1.06 \pm 0.10) \times 10^{-31}$	$(2.18 \pm 0.40) \times 10^{-30}$
4217–5623	$(3.82 \pm 1.71) \times 10^{-32}$	$(4.31 \pm 0.49) \times 10^{-32}$	$(6.50 \pm 2.34) \times 10^{-31}$
5623–10000	$(1.06 \pm 0.14) \times 10^{-32}$	$(1.07 \pm 0.16) \times 10^{-32}$	$(2.20 \pm 0.68) \times 10^{-31}$
10000–23714	$(1.35 \pm 0.15) \times 10^{-33}$	$(1.68 \pm 0.24) \times 10^{-33}$	$(1.72 \pm 0.92) \times 10^{-32}$
23714–100000	$(4.62 \pm 6.52) \times 10^{-35}$	$(9.55 \pm 3.50) \times 10^{-35}$	$(1.46 \pm 1.22) \times 10^{-33}$

Notes. Errors are statistical only.

^a $\text{MeV}^{-1} \text{s}^{-1} \text{sr}^{-1}$ per H atom.

^b $\text{MeV}^{-1} \text{s}^{-1} \text{sr}^{-1} (2 \times 10^{20} \text{cm}^{-2} (\text{K km s}^{-1})^{-1})^{-1}$.

^c $\text{MeV}^{-1} \text{s}^{-1} \text{sr}^{-1} (2 \times 10^{20} \text{mag})^{-1}$.

There is a problem with the color temperature correction of the map by Schlegel et al. (1998) around the OB associations in the Orion A and B clouds, and thus $E(B - V)_{\text{res}}$ value is negative in these points. We masked out these pixels in the $E(B - V)_{\text{res}}$ map by setting the corresponding values to zero.

The results for A_i (H I) and B_i (two normalizations, one for W_{CO} and the other for the “dark gas”) in Equation (1) are listed after combining the highest 10 energy bins into three bins in Table 3. The distribution of the gamma-ray counts associated with H₂-template-3, the sum of the counts associated with W_{CO} and the “dark gas,” is given in Figure 3(d). The correlation between the extracted gamma-ray counts and the model counts improves as shown in Figure 4(c), bringing the correlation coefficients to 0.99, 0.99, 0.97, and 0.98, for Orion A Region I, Region II, Orion B, and the sum of the three regions, respectively. The improvement in the correlation, or equivalently in the spatial fit, comes from inclusion of $E(B - V)_{\text{res}}$ which has the largest contribution in the Orion A Region I seen in Figure 2(c).

3.2.4. Summary of the Spatial Fits

The relative likelihoods of the spatial fits with Equation (1) in the ROI are compared among the three H₂ templates in Figure 5 for the 22 energy bins. The “dark-gas” template (H₂-template-3) gives the best fit in almost all energy bins and the 3- X_{CO} template (H₂-template-2) gives the second best result. The improvements relative to H₂-template-1 are statistically significant.

The residuals of the fits with the three templates in the ROI are given in Figure 6. The rectangular boundaries of the three Orion regions shown in Figures 3(b)–(d) are replicated in the figure. The residuals are significant within the Orion regions for H₂-template-1 (Figure 6(a)) but not for the other two templates (Figures 6(b) and (c)), which is consistent with the improvement we saw in Figure 4. The difference in the residuals for H₂-template-2 and H₂-template-3 in the Orion regions is not significant relative to the systematic uncertainty discussed in the next subsection. We find that the large improvement H₂-template-3 has brought relative to H₂-template-2 in Figure 5 comes primarily from outside of the three Orion regions, especially in the Monoceros R2 region and in the northern region

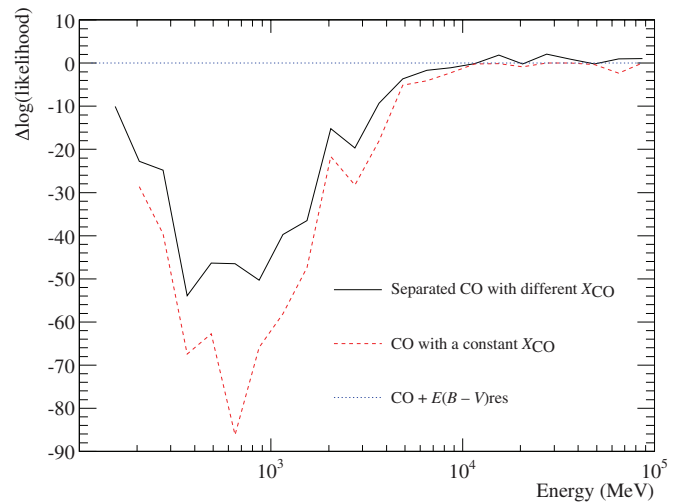


Figure 5. Difference in log(Likelihood) between the spatial fit using H₂-template-3 (dotted line) and either that with H₂-template-1 (dashed line) or that with H₂-template-2 (solid line) in the ROI for the 22 energy bins. Note that the lines are drawn between the data points only to guide the eye.

(A color version of this figure is available in the online journal.)

adjacent to the Orion B: the template adds “dark gas” in that part whereas the other templates only modify the three Orion regions.

The value of X_{CO} has been calculated by the H₂/H I method by taking the ratio of B_i to $2A_i$ for the parts associated with W_{CO} in the H₂ templates and listed in Table 2. In the pionic method of evaluating X_{CO} , however, the pionic component must be extracted out of the gamma-ray spectrum associated with the H₂ template as will be described in Section 3.3. We will discuss the systematic errors in evaluating X_{CO} and possible interpretations of the results in Section 4.

3.3. Analyses of Spectra

The spectra associated with the H I and H₂-template-1, with the H I and H₂-template-2, and with the H I and H₂-template-3 are obtained by assembling the fitted results for the respective

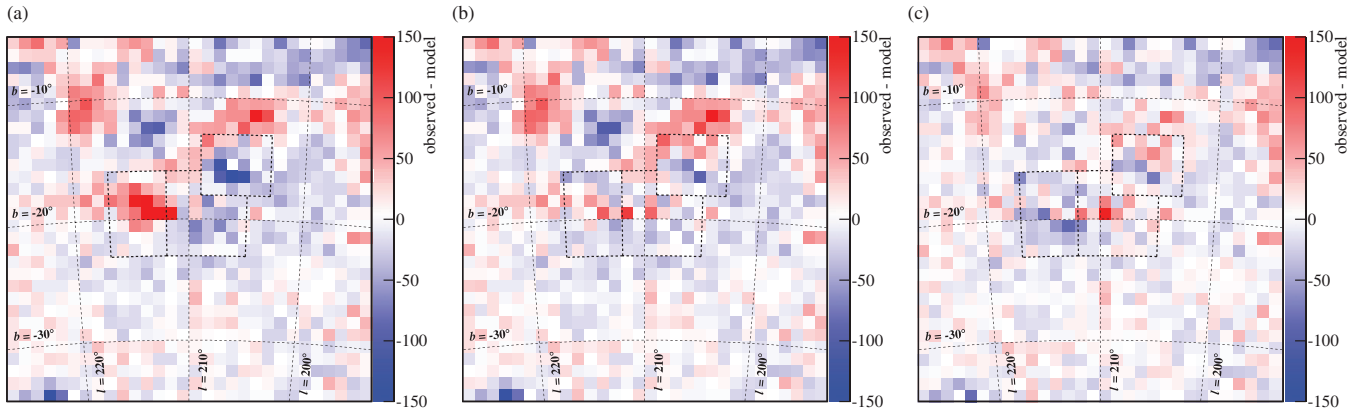


Figure 6. Residue in the energy-summed gamma-ray counts of the spatial fit with H₂-template-1 (a), H₂-template-2 (b), and H₂-template-3 (c), binned in 1×1 deg² pixels. The black dotted lines show the boundaries of the three regions, Orion A Region I, II, and Orion B.

(A color version of this figure is available in the online journal.)

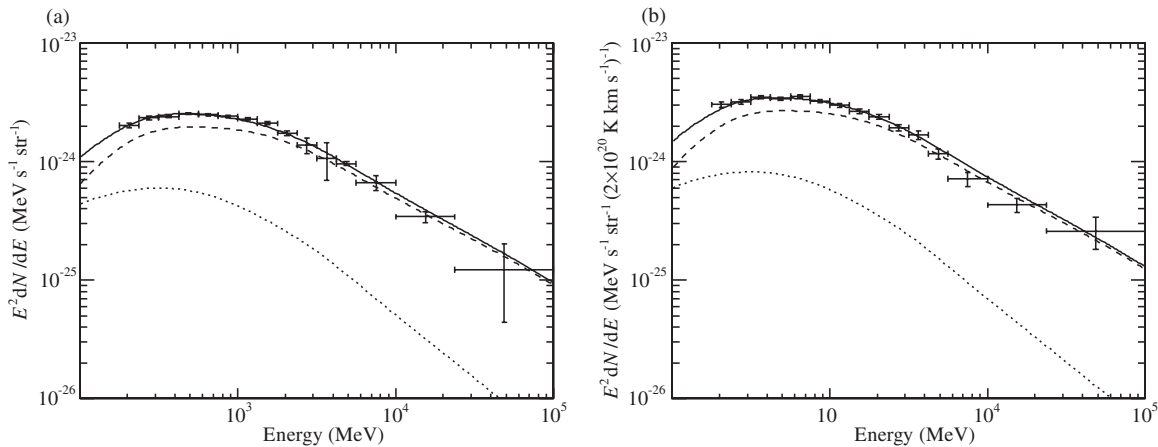


Figure 7. Spectral energy densities (SEDs) associated with local H I ($T_S = 125$ K assumed) (a) and that associated with H₂-template-1 (b). The lines are total (solid), bremsstrahlung (dotted), and pion decay (dashed). The CR spectral shape and electron-to-proton ratio at the Orion clouds were fixed to those used by GALPROP. The vertical axes are normalized to the column density of H I in unit of 1 cm^{-2} for (a) and to $2 \times X_{\text{CO}}$ in unit of $10^{20} \text{ cm}^{-2} (\text{K km s}^{-1})^{-1}$ for (b). The energy bins between no. 13 and no. 22 are combined to wider energy bins. Vertical bars represent statistical errors. Note that the spectral fit to H I is not used in evaluating X_{CO} .

templates, A_i and B_i , as shown in Figures 7, 8, and 9, respectively. The spectra are fitted as a sum of the pionic and bremsstrahlung components. The gamma-ray spectra associated with the spatial templates (H I, IC, isotropic, and sum of $X_{\text{CO}} \times W_{\text{CO}}$) are plotted for the three Orion regions in Figures 10(a) and (b). We analyze for the gamma rays associated with the three H₂ templates in this subsection.

3.3.1. Fit with Gamma-ray Emission Models

The spectral template of pionic gamma rays has been calculated by convolving the gamma-ray inclusive cross-section for $p-p$ interaction parameterized by Kamae et al. (2006) and the CR proton spectrum predicted by GALPROP at the Orion clouds.⁷⁵ The proton flux is predicted in the Orion clouds ($R = 8.8$ kpc, $Z = -0.14$ kpc) to be $\sim 8\%$ smaller than that at the solar system ($R = 8.5$ kpc, $Z = 0.0$ kpc) where the

⁷⁵ In GALDEF 54_77Xvarh7S, the CR proton flux was artificially multiplied by 1.15 to reproduce gamma-ray observations by *Fermi*. The factor originates from the underestimate of gamma-ray emissivity for He and heavier atoms in the interstellar medium (ISM) in GALPROP. Instead of using the 1.15 correction factor, we combined the calculation by Gaisser & Schaefer (1992) for contributions from CR He and heavier atoms, and the calculation by Mori (2009) for heavier atoms in the ISM. Hence, the total gamma-ray emissivity per H atom is 1.70 times larger than that for $p-p$ collisions only. The difference between the total gamma-ray emissivity in the two literatures is $\sim 5\%$, which is taken into account in the systematic uncertainty.

GALPROP proton spectrum has been determined by the CR data taken at the Earth. The value at the Orion clouds is consistent with that determined using the gamma rays from the local H I (Abdo et al. 2009b). The good fit to the data seen in Figures 7–9 supports GALPROP’s prediction of CR spectral shape in the Orion region and the overall modeling of Equation (1).

Bremsstrahlung emission induced by CR electrons interacting with gas is calculated in GALPROP using recent bremsstrahlung calculations (Strong & Moskalenko 1998; Strong et al. 2000, and references therein). The electron injection spectrum in our GALPROP calculation had been adjusted to reproduce, approximately, the power-law index of the electron spectrum measured by the *Fermi*-LAT (Abdo et al. 2009d). In addition, the normalization of the spectrum is adjusted to reproduce the LAT observed gamma-ray flux at a low-energy band. In the spectral fits described below, we kept the electron-to-proton ratio, or equivalently the bremsstrahlung-to-pion ratio, fixed to the value given in GALPROP. When we refer to the gamma-ray emissivity per atom or molecule, we do not differentiate the underlying processes, but rather the sum of the bremsstrahlung and pionic contributions.

The spectral fit of the H I component is reasonable for all three H₂ templates ($\chi^2 = 17.7, 9.9,$ and 17.1 for /dof = 14, respectively) as shown in Figures 7(a), 8(a), and 9(a). Our pionic

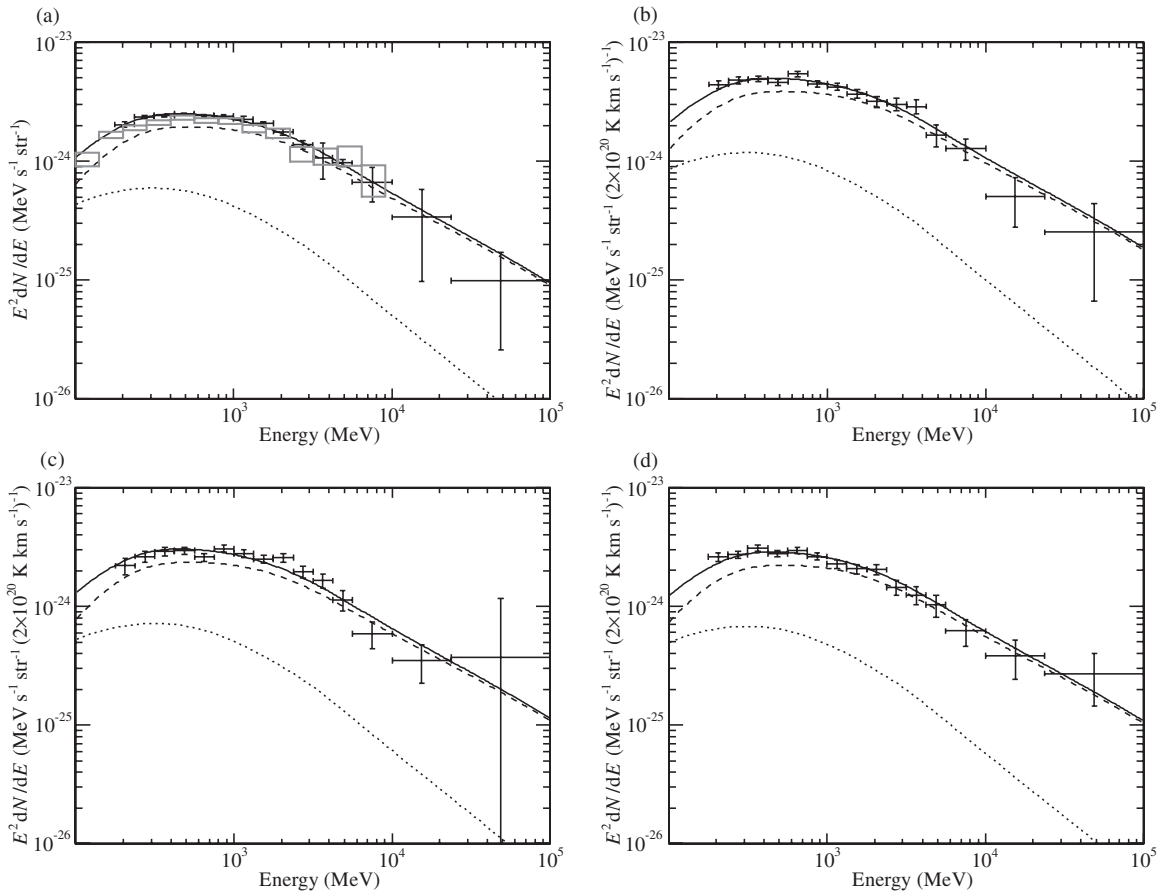


Figure 8. Spectral energy density (SED) associated with local H I ($T_S = 125$ K assumed) (a), Orion A Region I (b), Region II (c), and Orion B (d) for the fit with H_2 -template-2. The corresponding SED obtained for the local H I (Abdo et al. 2009b) is shown by gray squares in (a). The assumption about the CR, the line legends, and the vertical axis units are the same as in Figure 7.

flux associated with H I is consistent with that obtained in the *Fermi* study on the local interstellar gas (Abdo et al. 2009b) as overlaid in Figure 8(a). We note however that there may be a small offset between the two as will be discussed later. The spectra associated with molecular clouds are also fitted well by the three H_2 templates as shown below.

The mass-to- W_{CO} ratio, X_{CO} , can be obtained by comparing the assumed pionic gamma-ray emissivity per H atom with the observed gamma-ray emissivity per W_{CO} as shown in Figures 7(b), 8(b), 8(d), and 9(b). The former is calculated in the unit of $\text{MeV}^{-1} \text{s}^{-1} \text{sr}^{-1}$, and the latter is measured in the unit of $\text{MeV}^{-1} \text{s}^{-1} \text{sr}^{-1} (2 \times 10^{20} \text{cm}^{-2} (\text{K km s}^{-1})^{-1})^{-1}$. Thus, $X_{CO}/2$ of the clouds is derived by dividing the latter by the former.

The results of the spectral fit for the H I component are not used to determine X_{CO} in the pionic method. The fits to the spectral components shown in Figures 7(a), 8(a), and 9(a) are only to check overall consistency of our analyses. Their normalizations are consistent within the uncertainty in the H I column density discussed in Section 4.

3.3.2. Spectra Obtained with H_2 -template-1

The fitted spectra are plotted as sums of pionic and bremsstrahlung emissions in Figures 7(a) and (b) for the H I spatial template and the H_2 -template-1 (Orion A Region I, II, and Orion B combined), giving χ^2/dof of 17.7/14 and 20.2/14, respectively.

We give the X_{CO} value obtained from the fitted pionic spectra in Table 2. Since the fit is substantially poorer than those for

H_2 -template-2 and 3 (see Figure 5), the value should be taken just as a reference value. For this reason, we do not quote systematic errors in the table.

3.3.3. Spectra Obtained with H_2 -template-2

The fitted spectra are plotted as sums of pionic and bremsstrahlung emissions in Figures 8(b)–(d) for Orion A Region I, II, and Orion B, giving χ^2/dof of 14.0/14, 18.5/14, and 10.6/14, respectively. The X_{CO} values obtained for the four regions from the fitted pionic spectra are given in Table 2.

The coefficient X_{CO} is significantly higher for Orion A Region I than for other regions, consistent with the slopes obtained in Section 3.2 in the pixel-by-pixel correlation study. This also can be seen in the X_{CO} obtained with the $H_2/\text{H I}$ method.

We note that the fraction of the H I component in the gamma-ray spectrum integrated in the three Orion regions is comparable to that associated with W_{CO} (see Figure 10(a)). This is because the solid angle subtended by the Orion molecular clouds is a small fraction of our three Orion regions in solid angle and the overall mass of atomic gas is greater.

3.3.4. Spectra Obtained with H_2 -template-3

The fitted spectra integrated over the W_{CO} and “dark-gas” components are shown in Figures 9(b) and (c). We give X_{CO} for the ROI from the fitted pionic spectrum in Table 2.

The X_{CO} obtained in fits with the W_{CO} can be compared with those obtained in similar analyses including the “dark-gas”

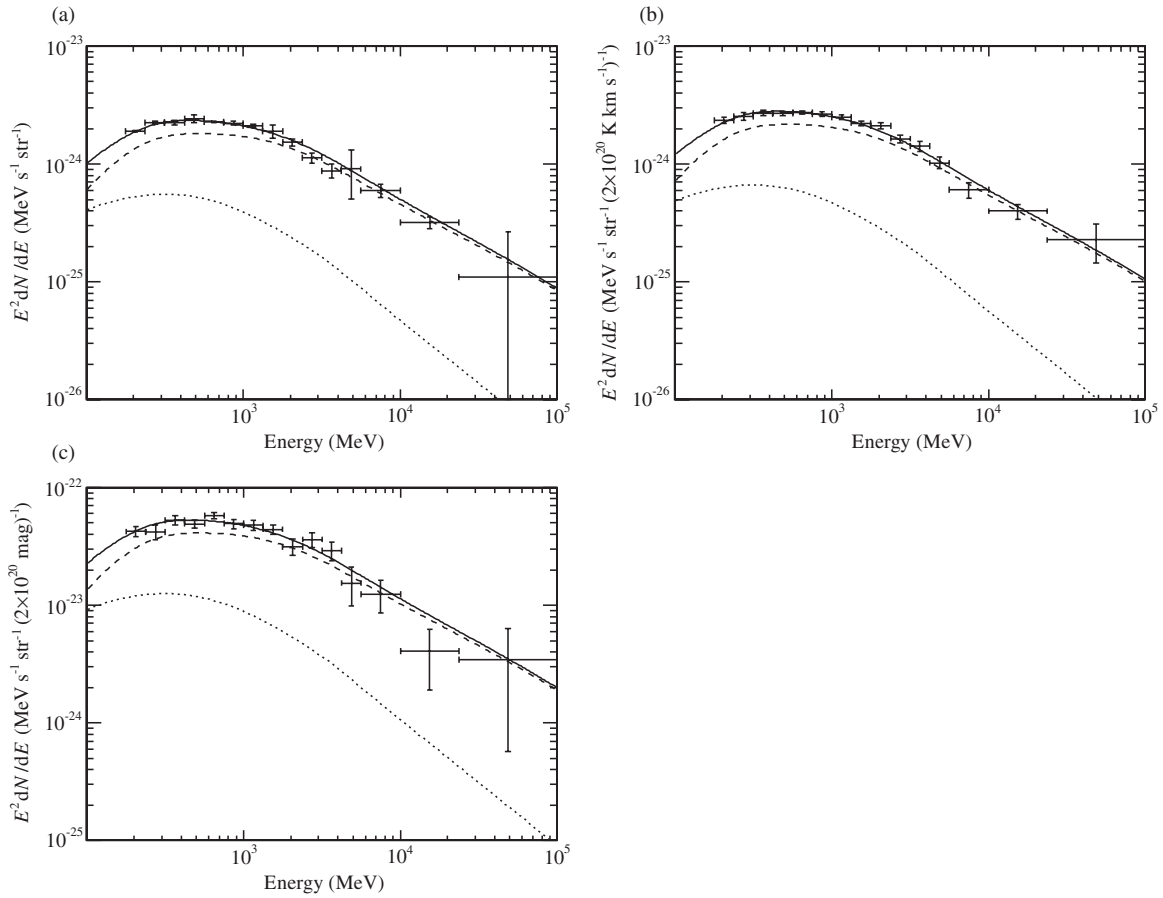


Figure 9. SED associated with local H I ($T_S = 125$ K assumed) (a), that associated with W_{CO} (b), and that associated with $E(B - V)_{\text{res}}$ (c) obtained with H₂-template-3. The line legends and vertical axis units are the same as in Figure 7.

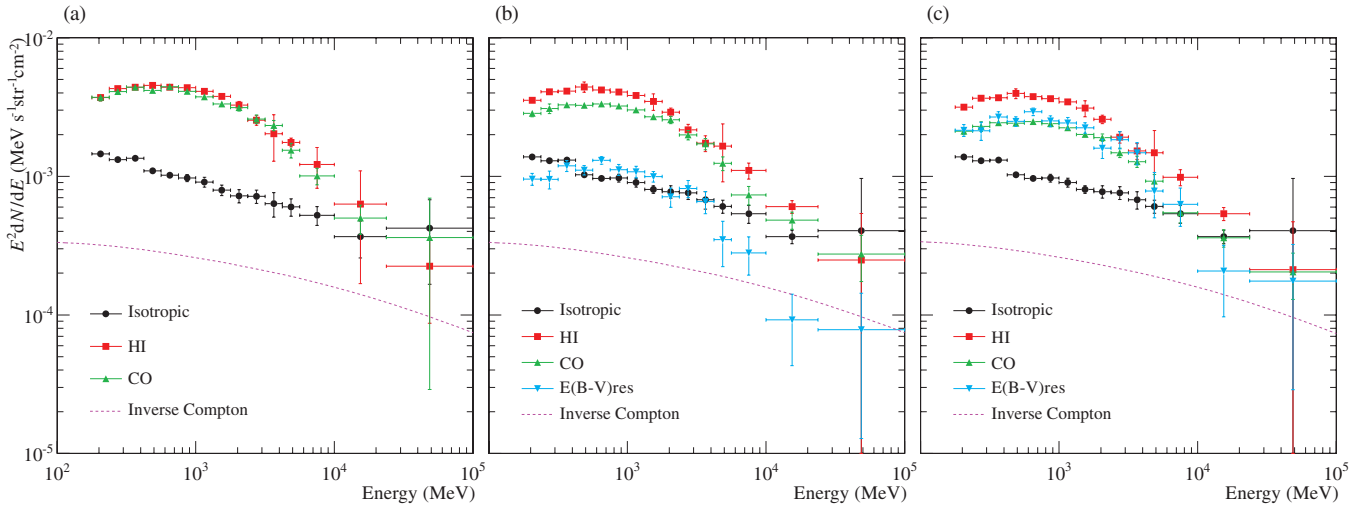


Figure 10. Gamma-ray spectra spatially associated with two H₂ templates in the three Orion regions marked in Figure 3(b): (a) the sum of the three regions obtained with H₂-template-2, (b) the sum of the three regions with H₂-template-3, and (c) Orion A Region I obtained with H₂-template-3. Black circles show the isotropic component, red squares HI, green upward triangles CO, and purple dashed line the inverse Compton. Blue downward triangles in (b) and (c) represent the spectra associated with $E(B - V)_{\text{res}}$.

(A color version of this figure is available in the online journal.)

template: 2.0×10^{20} (in the local arm), 1.9×10^{20} (the Perseus arm), and 0.87×10^{20} (the Gould Belt) in the same unit as above (Ackermann et al. 2010; Abdo et al. 2010c).

The spectrum associated with the “dark-gas” component is similar in shape to that associated with W_{CO} but about half as intense (Figure 10(b)). The two spectral energy densities (SEDs) become comparable in Orion A Region I as seen in Figure 10(c).

The “dark gas” dominates over W_{CO} in the pixels near the high-longitude end of Orion A and eventually W_{CO} diminishes in the pixels beyond them toward higher longitude.

Our X_{CO} measurements given in Table 2 can be compared with those determined using the gamma-ray flux from the Orion–Monoceros complex measured with EGRET: $(1.35 \pm 0.15) \times 10^{20} \text{ cm}^{-2} (\text{K km s}^{-1})^{-1}$ (Digel et al. 1999). We

note there were no Galactic CR propagation models such as GALPROP nor CR measurements as precise as are available now: X_{CO} was determined by the $\text{H}_2/\text{H I}$ method and it compares well with the single X_{CO} value of 1.36 ± 0.02 obtained with the H_2 -template-1.

3.4. Total Masses of Orion A and B

The distance from the Sun to the Orion Nebula (M42) inside the Orion A has recently been measured by parallax to be 389^{+24}_{-21} pc (Sandstrom et al. 2007), 414 ± 7 pc (Menten et al. 2007), 437 ± 19 pc (Hirota et al. 2007), and 419 ± 6 pc (Kim et al. 2008). We adopted 400 pc as the distance to the Orion A and B clouds and used the total pionic gamma-ray fluxes obtained above to get the total masses of Orion A and B outside.⁷⁶

Mass estimation using H_2 -template-2.

$$M_{\text{A}} = (74.5 \pm 1.3) \times 10^3 M_{400}$$

$$M_{\text{B}} = (33.5 \pm 0.7) \times 10^3 M_{400},$$

where

$$M_{400} = \left(\frac{d}{400 \text{ pc}} \right)^2 \times M_{\odot}, \quad (2)$$

and d is the distance to the clouds. We will discuss the systematic uncertainties in the next section.

Mass estimation using H_2 -template-3. Addition of the “dark gas” changes the estimation of the Orion A and B masses by about 10%.

$$M_{\text{A},\text{WCO}} = (55.1 \pm 0.8) \times 10^3 M_{400}$$

$$M_{\text{A},\text{Dark}} = (27.6 \pm 0.7) \times 10^3 M_{400}$$

$$M_{\text{B}} = (36.0 \pm 0.5) \times 10^3 M_{400}.$$

The total mass of Orion A ($\equiv M_{\text{A},\text{WCO}} + M_{\text{A},\text{Dark}}$) is $(82.7 \pm 1.1) \times 10^3 M_{400}$. The Orion A mass has been estimated by Wilson et al. (2005), assuming $X_{\text{CO}} = 1.8 \times 10^{20} \text{ cm}^{-2} (\text{K km s}^{-1})^{-1}$ (Dame et al. 2001), to be $M_{\text{A}} = 91.7 \times 10^3 M_{400}$. The mass has been estimated separately for Orion A Regions 1, 2, 3, and NGC 2149 in Wilson et al. (2005). Our Orion A (Region I and II) includes their Regions 1, 2, and 3 but overlaps only partially with NGC 2149. Considering the breadth of the PSF and the limited statistics of the data, we could not determine how much of NGC 2149 overlaps our Orion Region I. If we assume about one-half of NGC 2149 is in our Orion Region I and the systematic error introduced by this ambiguity is half of the NGC 2149 mass estimated by Wilson et al. (2005), the Orion A mass to be compared becomes $M_{\text{A}} = (86.3 \pm 5.4) \times 10^3 M_{400}$. The Orion B region is more complex and such a comparison is very difficult.

4. DISCUSSION

Although the Orion clouds lie away from the Galactic plane and subtend relatively small solid angle, many Galactic and extragalactic sources contribute to the ROI through the large PSF of the *Fermi*-LAT.

We have analyzed the observed data to extract the intensity associated with the molecular clouds, the three Orion regions in particular, by using the three H_2 templates made from W_{CO} on

the three different assumptions for each of the 22 energy bins. The ratio of the normalization factors for H I and H_2 , $A_i/2B_i$, gives the conversion factor of W_{CO} to the mass column density, X_{CO} (the $\text{H}_2/\text{H I}$ method). For this, the H I mass column density must be well understood from the radiative transfer of the H I line and the CR spectrum must be constant in the ROI.

In the second method (the pionic method), X_{CO} is determined by comparing the observed pionic gamma-ray intensities with those expected from the CR spectrum at the Orion clouds and the pionic gamma-ray production cross-section. For this, we have to know the absolute CR spectrum and flux, the instrument response function (IRF), and the pionic gamma-ray production cross-section, in particular the pionic gamma-ray contribution from metals in CR and ISM.

In the subsections to follow, we evaluate uncertainties and possible systematic errors in the analyses, especially in evaluating X_{CO} in the three Orion regions. We then summarize the results obtained in this paper and present possible interpretations thereon.

4.1. Possible Systematic Errors in the Analyses

Systematic errors that affect the correlation measurements between gamma-ray intensities and W_{CO} are discussed in two categories: the first one applies commonly to the three Orion regions and the second affects the relation differently in the three regions.

4.1.1. CR Intensity at the Orion Clouds

Uncertainty in the fluxes and spectra of CRs, in particular those of protons, can affect in both categories. The Galactic CR protons that produce pions in our energy range remain in our Galaxy longer ($\sim 5 \times 10^7$ yr) than electrons ($\sim 7 \times 10^6$ yr) (Lee et al. 2011) and their flux variation within the Galaxy is believed to be predicted well by GALPROP. We note that the CR source distribution, the Galaxy size, and the CR diffusion coefficient are the important inputs to GALPROP. Using the CR spectrum measured at the Earth, we have calculated the CR spectrum in the Orion region for the two choices of the CR source distributions and the three choices of Galactic halo heights (2, 4, and 10 kpc) used in a GALPROP-based study by Lee et al. (2011). The CR spectrum does not change more than $\sim 2\%$ from the value used here as long as it is constrained to the measurements at the Earth and to reproduce the Galactic diffuse gamma-ray intensities measured by the *Fermi*-LAT (see Lee et al. 2011). We also note that the gamma-ray spectrum from the local H I (typical distance < 1 kpc) is consistent with the CR proton flux being within $\sim 10\%$ of that at the Earth (Abdo et al. 2009b).

CRs could be accelerated in the clouds and/or prevented from penetrating into their cores by embedded magnetic field. We first note that there are no strong non-thermal X-ray source nor radio supernova remnants found in the clouds (Feigelson et al. 2002, and references therein). Therefore, no appreciable CR acceleration is likely to be taking place in the Orion clouds. The good linear correlation between W_{CO} and gamma-ray intensity seen in all three Orion regions (Figure 4(a)) confirms that the CRs effective in producing pions (kinetic energy > 1 GeV) are penetrating well inside the higher-density parts of the clouds.

Based on these observations, we assume that the CR flux in the Orion region is 8% lower than that at the Earth with possible systematic error of $\pm 10\%$ due mostly to disagreement among recent CR measurements at the Earth and solar demodulation uncertainties.

⁷⁶ We note that the spatial extent of Orion B defined here is significantly different from that used in Wilson et al. (2005) because we are unable to separate Orion B from the complex cloud structures behind due to the broad PSF of the LAT.

Uncertainty in the CR flux at the Orion clouds contributes directly to the systematic error in the pionic method but indirectly in the H_2/HI method. In the former, the absolute CR intensity is assumed to be known while the CR intensity is assumed to be the same in the local HI region and the molecular clouds in the latter.

4.1.2. Uncertainty in the Instrument Response Functions

The uncertainty in the absolute calibration of the LAT effective area can also introduce error of the first kind. The effective areas were derived based on Monte Carlo studies of the LAT, checked against beam tests at accelerators (Abdo et al. 2009a; Atwood et al. 2009). Comparisons between flight data and Monte Carlo studies have been made to quantify the systematic uncertainty in the effective area (Abdo et al. 2009f). At present, we estimate this systematic error to be 10% at 100 MeV, 5% at 500 MeV, and 20% at 20 GeV.

The systematic error in the absolute energy scale has been estimated as +5%/−10% (Abdo et al. 2009d). We have refitted X_{CO} after artificially shifting the energy scale by +5% and by −10%: the number of pionic gamma rays changes less than +1%/−8% for all three Orion regions with all three H_2 templates. We include this possible error due to the uncertainty in the energy calibration when assessing the overall systematic error.

The pionic method is affected directly by the uncertainty in the IRF while the H_2/HI method is insensitive because it affects the denominator and numerator similarly.

4.1.3. Uncertainty in the Spin Temperature of HI

In converting the observed 21 cm line emission intensity (Kalberla et al. 2005) to the HI column density, T_S was assumed to be 125 K. The range of T_S measured in the local HI gas varies broadly between 90 K and 400 K (e.g., Mohan et al. 2004a, 2004b, and references therein) while we have assumed a likely range for our ROI to be between 90 K and 250 K.

We refitted the *Fermi* data in the ROI with these two extreme T_S values with H_2 -template-2 and 3. We then calculated X_{CO} by dividing B_i by $2A_i$ in Equation (1), or by extracting the pion component in the spectra. The deviations of X_{CO} from those obtained with T_S of 125 K are taken into account in the systematic errors given in Table 2. The large systematic errors for X_{CO} on $B_i/2A_i$ (Column 3) enter via $2A_i$ which depends on the absolute calibration of the HI gas density or T_S in the local HI. The pionic method uses the product of the CR intensity and $pp \rightarrow \gamma$ cross-section in place of $2A_i$ and is less directly affected by the uncertainty in HI gas density or T_S of the local HI, although the uncertainties can have a small indirect effect through the overall spatial fitting. This effect is much smaller than the overall systematic error and negligible. We note that there is some discrepancy between the gamma-ray spectra associated with HI in the ROI and the local HI (Abdo et al. 2009b) as seen in Figure 8.

4.1.4. Effect of Overlapping Point Source Candidates

We have not included the five sources overlapping with the Orion clouds (Section 3.1.4) because they are all classified as “potentially confused with interstellar diffuse emission or perhaps spurious” (Abdo et al. 2010b). To investigate their potential contribution we repeated the analysis including these sources with the fluxes and spectra listed in the First *Fermi* LAT Catalog. The fit with the pionic method gives the following X_{CO} in unit of $\text{cm}^{-2} (\text{K km s}^{-1})^{-1}$: $(2.29 \pm 0.05) \times 10^{20}$ for

Orion Region I, $(1.16 \pm 0.05) \times 10^{20}$ for Orion Region II, and $(1.24 \pm 0.04) \times 10^{20}$ for Orion B. They are 2%, 19%, and 8% less than those obtained without these point-source candidates. In the present study, we assume they are artifacts and add +0%/−2%, +0%/−19%, and +0%/−8% to the overall systematic error in the three regions.

4.1.5. Overall Error

For the H_2/HI method, the uncertainty in the HI mass density ($\sim 20\%$) due mostly to the uncertainty in T_S dominates the systematic error. Other contributions include the overlapping “c” sources (+0%/−2%, +0%/−19%, and +0%/−8%) and variation in the CR intensity within ~ 1 kpc or between HI and the molecular clouds ($\pm 5\%$), making the total systematic errors for the three Orion regions to +25%/−28%, +25%/−44%, and +25%/−33% as given in Column 3 of Table 2.

For the pionic method, the overall systematic error in determining X_{CO} comes from the uncertainty in the IRF including that due to the energy calibration uncertainty ($\pm 10\%$), unknown contributions of the overlapping sources (+0%/−2%, +0%/−19%, and +0%/−8%), uncertainty in the CR intensity ($\pm 10\%$), uncertainty in the pp pion production cross-section ($\pm 5\%$), and uncertainty in the contribution from heavier nuclei ($\pm 5\%$). We conservatively quote the linear sum of these combinations as the possible systematic error for the three Orion regions, which are +30%/−32%, +30%/−49%, and +30%/−38%, as given in Column 5 of Table 2.

The systematic errors that can affect X_{CO} differently in the three Orion regions are variation in the CR intensity within ~ 1 kpc ($\pm 5\%$) and the overlapping sources. The overall error of this kind is conservatively estimated to be the linear sum of the two, +5%/−7%, +5%/−24%, and +5%/−13%.

4.2. Gamma-Ray Intensity and $E(J - H)$

The line-of-sight visual attenuation, A_V , are often used as a gas-mass tracer in theory-based studies of the CO fraction in all molecules including carbon and hydrogen (e.g., Burgh et al. 2010; Wolfire et al. 2010; Glover et al. 2010, and references therein). To calibrate crudely our mass column density with A_V used in these theory-based analyses, we have related the gamma-ray counts on the horizontal axes of Figure 4 and $E(J - H)$ in the three Orion regions measured by Dobashi (2011). We note that the atomic and molecular components are assumed to be contained within a fixed length (e.g., 20 pc) along the line of sight in the theory-based analyses while the components are measured as column densities integrated over unknown lengths along the line of sight in observations. Moreover, $E(J - H)$ is known to trace the H_2 gas but also pick up some HI gas through dust mixed with it. Hence, the cross-calibration works at best crudely and only in the regions of clouds where the H_2 longitudinal distribution is well confined and the H_2 volume density dominates over that of HI. Despite these uncertainties, it is important that our measurements be compared with theory-based analyses.

We found good linear relations for the pixels with high gamma-ray counts (> 300 per deg^2) in all three Orion regions and could correlate the gamma-ray count scale on the horizontal axes of Figure 4 to $E(J - H)$ assuming $A_V = R_{V-EJH} \times E(J - H)$. The R_{V-EJH} has been determined observationally and its value ranges between 7.8 (Dobashi 2011) and 10.9 (Cardelli et al. 1989). The highest point in our count map is ~ 700 per pixel in Orion A Region II where H_2 concentration is highest and

the corresponding value of A_V is ~ 5 when averaged over $1 \times 1 \text{ deg}^2$ pixels for an assumed value of $R_{V-EJH} = 7.8$. So $A_V = 5$ on the horizontal axes of Figures 5 and 6 in Glover et al. (2010) corresponds crudely to ~ 700 counts per pixel assuming H_2 is well confined (e.g., to ~ 20 pc) along the line of sight.

4.3. Summary of the Results

The results obtained in the present work are significant beyond the estimated systematic errors. They are as follows:

1. Linearity holds between mass density associated with the Orion clouds and W_{CO} : as discussed in Section 3.2 and shown in Figure 4, our results suggest that CRs penetrate to all translucent part of the clouds. Possible shielding of CRs discussed in Aharonian (2001) does not apply to most parts of the Orion clouds.
2. The X_{CO} factors calculated with the pionic method and with the H_2/HI method differ by $\sim 15\%$ but agree within the estimated systematic error (Table 2). The difference can be explained by uncertainties in the column densities of HI and calculation of gamma-ray emissivity per HI atom.
3. The X_{CO} factor obtained with the H_2 -template-2 is found to be larger by $\sim 40\%$ – 60% in Orion A Region I than Orion A Region II and Orion B for the two methods. The difference is much larger than the systematic error that can affect the X_{CO} factor differently in the three Orion regions (Table 2).
4. In the “dark-gas” scenario, the added “dark gas” accounts for the majority of the gas not traced by W_{CO} . One X_{CO} factor can then describe the W_{CO} -traced H_2 distribution in the ROI.

4.4. Interpretation of Our Results on X_{CO}

Historically, the relation between $N(\text{H}_2)$ to W_{CO} has been considered to depend on the environment around the molecular cloud. The environmental factors discussed in the literature are as follows:

Metallicity. This possibility has been discussed in the literature since the late 1980s (e.g., Elmegreen 1989; Bolatto et al. 1999). According to an empirical formula proposed to relate X_{CO} to $[\text{O}/\text{H}]$ (Wilson 1995; Arimoto et al. 1996), the metallicity must be ~ 2 times higher in Orion A Region I to account for the observed difference in X_{CO} between Region I and II, which is unlikely according to Galactic-scale measurements (e.g., Esteban et al. 2005). We note that metallicity is generally considered to be an important environmental factor influencing the H_2 -to- HI ratio.

Overlapping HI clumps. Compact HI clouds with angular diameters of 1° – 2° have been found in various Galactic locations (e.g., Braun & Strom 1986; Kavars et al. 2003; Lee et al. 2008). A new reanalysis of the LAB HI survey shows no such concentration detected at the sensitivity level of the present study overlapping with the Orion A and B (Kalberla et al. 2010).

Low-density H_2 not traced well by W_{CO} . Existence of diffuse H_2 gas not traced well by W_{CO} has been discussed in the literature cited in Section 1 and *Fermi* analyses are bringing the discussion to a quantitative level (Ackermann et al. 2010). We refer to the following recent works on the H_2 and CO fractions and try to interpret our results:

1. Burgh et al. (2010) have studied the fractions based on *Hubble Space Telescope* observations and characterized the X_{CO} dependency on $N(\text{H}_2)$.

2. Wolfire et al. (2010) have studied chemical composition of a model cloud theoretically and found that CO becomes depleted because of photodissociation in the periphery where the gas density decreases.
3. Glover et al. (2010) have studied the time-dependent H_2 and CO fractions in clouds through computer simulations and found X_{CO} increases sharply where $N(\text{H}_2)$ decreases for $A_V < 3.5$.

All of the above studies predict that the $\text{CO}/(\text{total C})$ fraction drops as the H_2 column density decreases, as toward the periphery of Orion A and B. However, the W_{CO} -to- H_2 relation and the abundance of H_2 -without-CO gas may be more complicated. For example, Ikeda et al. (2002) found that $N(\text{C I})/N(\text{CO})$ increases to high values along all of the peripheries whereas we find Region I of Orion A to be more abundant in CO-depleted gas than Region II. The prediction that X_{CO} increases sharply in regions $A_V < 3.5$ by Glover et al. (2010) is consistent with our finding that the “dark gas” is concentrated in the high-longitude end of Orion A where W_{CO} becomes low.

5. CONCLUSION

We have reported on the first 21 months’ observations of Orion A and B with the *Fermi Gamma-ray Space Telescope* in the energy band between ~ 178 MeV and ~ 100 GeV. We have measured the mass column density distribution within the clouds at the angular scale of the instrument PSF using the $pp \rightarrow \gamma$ production cross-section accurately calibrated at accelerators as well as using the gamma-ray emissivity of the local HI gas. We found with the pionic method that a linear relation holds between mass density and W_{CO} with $X_{\text{CO}} = 2.34, 1.43,$ and $1.35 \times 10^{20} \text{ cm}^{-2} (\text{K km s}^{-1})^{-1}$ with a systematic uncertainty of $+5\%/-7\%$, $+5\%/-24\%$, and $+5\%/-13\%$ (relative in the three regions), and $+30\%/-32\%$, $+30\%/-49\%$, and $+30\%/-38\%$ (absolute) for Orion A Region I, Region II, and Orion B, respectively. These values are consistent with the X_{CO} values determined with the more traditional H_2/HI method ($X_{\text{CO}} = 1.97, 1.20,$ and $1.14 \times 10^{20} \text{ cm}^{-2} (\text{K km s}^{-1})^{-1}$) within our overall systematic error. This implies that Galactic CRs are penetrating into most parts of the clouds. The analyses also included the “dark gas” (Grenier et al. 2005) not traced by CO or HI. We found that the gamma-ray flux associated with the “dark-gas” spatial template exceeds that associated with the W_{CO} template in Orion A Region I. The situation is reversed in Region II and in Orion B. This is generally consistent with the fit finding a higher X_{CO} value for Orion Region I in the absence of the dark-gas template.

We have interpreted the increase in X_{CO} and “dark gas” fraction in Orion A Region I in the light of recent studies of the relation between the H_2 and CO fractions by Burgh et al. (2010), Wolfire et al. (2010), and Glover et al. (2010). X_{CO} is expected to increase rapidly as the gas column density decreases to $A_V \sim 3.5$ or less (Glover et al. 2010). The mass column density we have measured in Region I corresponds to $A_V < 4$, close to the predicted threshold for onset of the nonlinearity predicted between W_{CO} and $N(\text{H}_2)$. The mass column density drops further ($A_V < 2$) toward the high Galactic longitude end of the Orion A where the gas becomes “dark” to W_{CO} , consistent with the predicted nonlinear relation.

The *Fermi*-LAT collaboration is continuing to reduce uncertainty in the IRF, identify extended gamma-ray sources, and improve the modeling of the Galactic-scale diffuse

gamma-ray emission. We expect the systematic uncertainties quoted in Section 4.1 to be reduced significantly through these efforts. The systematic uncertainty in the CR spectra and the H I mass density also will be reduced when the data from new experiments and surveys become available. The present analyses can then be updated to a higher precision and the relation among W_{CO} and the gas mass density characterized further for various molecular clouds in the Galaxy.

The *Fermi*-LAT collaboration acknowledges generous ongoing support from a number of agencies and institutes that have supported both the development and the operation of the LAT as well as scientific data analysis. These include the National Aeronautics and Space Administration and the Department of Energy in the United States, the Commissariat à l'Énergie Atomique and the Centre National de la Recherche Scientifique/Institut National de Physique Nucléaire et de Physique des Particules in France, the Agenzia Spaziale Italiana and the Istituto Nazionale di Fisica Nucleare in Italy, the Ministry of Education, Culture, Sports, Science and Technology (MEXT), High Energy Accelerator Research Organization (KEK) and Japan Aerospace Exploration Agency (JAXA) in Japan, and the K. A. Wallenberg Foundation, the Swedish Research Council and the Swedish National Space Board in Sweden.

Additional support for science analysis during the operations phase is gratefully acknowledged from the Istituto Nazionale di Astrofisica in Italy and the Centre National d'Études Spatiales in France.

REFERENCES

- Abdo, A., Ackermann, M., Ajello, M., et al. 2009a, *Astropart. Phys.*, **32**, 193
- Abdo, A., Ackermann, M., Ajello, M., et al. 2009b, *ApJ*, **703**, 1249
- Abdo, A., Ackermann, M., Ajello, M., et al. 2009c, *ApJS*, **183**, 46
- Abdo, A., Ackermann, M., Ajello, M., et al. 2009d, *Phys. Rev. Lett.*, **102**, 181101
- Abdo, A., Ackermann, M., Ajello, M., et al. 2009e, *Phys. Rev. Lett.*, **103**, 251101
- Abdo, A., Ackermann, M., Ajello, M., et al. 2010a, *Phys. Rev. Lett.*, **104**, 101101
- Abdo, A., Ackermann, M., Ajello, M., et al. 2010b, *ApJS*, **188**, 405
- Abdo, A., Ackermann, M., Ajello, M., et al. 2010c, *ApJ*, **710**, 133
- Abdo, A., Ackermann, M., Atwood, W. B., et al. 2009f, *ApJ*, **696**, 1084
- Ackermann, M., Ajello, M., Baldini, L., et al. 2010, *ApJ*, **726**, 81
- Ade, P. A. R., Aghanim, N., Arnaud, M., et al. (Planck Collaboration) 2011, *A&A*, **536**, A19
- Aharonian, F. A. 2001, *Space Sci. Rev.*, **99**, 187
- Arimoto, N., Sofue, Y., & Tsujimoto, T. 1996, *PASJ*, **48**, 275
- Atwood, W. B., Abdo, A. A., Ackermann, M., et al. 2009, *ApJ*, **697**, 1071
- Balakrishnan, N., Yan, M., & Dalgarno, A. 2002, *ApJ*, **568**, 443
- Bally, J. 2008, in *Handbook of Star Forming Regions, Vol. I, The Northern Sky*, ed. B. Reipurth (San Francisco, CA: ASP), 459 (arXiv:0812.0046)
- Beichman, C. A., Neugebauer, G., Habing, H. J., et al. 1988, *Infrared Astronomical Satellite (IRAS) Catalogs and Atlases*, NASA RP-1190
- Bell, T. A., Roueff, E., Viti, S., & Williams, D. A. 2006, *MNRAS*, **371**, 1865
- Bell, T. A., Viti, S., & Williams, D. A. 2007, *MNRAS*, **378**, 983
- Bergin, E. A., & Tafalla, M. 2007, *ARA&A*, **45**, 339
- Bertsch, D. L., Dame, T. M., Fichtel, C. E., et al. 1993, *ApJ*, **416**, 587
- Bloemen, J. B. G. M., Caraveo, P. A., Hermsen, W., et al. 1984, *A&A*, **139**, 37
- Bolatto, A. D., Jackson, J. M., & Ingalls, J. G. 1999, *ApJ*, **513**, 275
- Braun, R., & Strom, R. G. 1986, *A&A*, **164**, 193
- Bronfman, L., Cohen, R. S., Alvarez, H., May, J., & Thaddeus, P. 1988, *ApJ*, **324**, 248
- Burgh, E. B., France, K., & Jenkins, E. B. 2010, *ApJ*, **708**, 334
- Burgh, E. B., France, K., & McCandliss, S. R. 2007, *ApJ*, **658**, 446
- Caraveo, P. A., Bennett, K., Bignami, G. F., et al. 1980, *A&A*, **91**, L3
- Cardelli, J. A., Clayton, G. C., & Mathis, J. S. 1989, *ApJ*, **345**, 245
- Cecchi-Pestellini, C., Bodo, E., Balakrishnan, N., & Dalgarno, A. 2002, *ApJ*, **571**, 1015
- Dame, T. M., Hartmann, D., & Thaddeus, P. 2001, *ApJ*, **547**, 792
- Dame, T. M., Ungerechts, H., Cohen, R. S., et al. 1987, *ApJ*, **322**, 706
- Dickman, R. L., Snell, R. L., & Schloerb, F. P. 1986, *ApJ*, **309**, 326
- Digel, S. W., Aprile, E., Hunter, S. D., Mukherjee, R., & Xu, F. 1999, *ApJ*, **520**, 196
- Digel, S. W., Hunter, S. D., & Mukherjee, R. 1995, *ApJ*, **441**, 270
- Dobashi, K. 2011, *PASJ*, **63**, S1
- Dobashi, K., Uehara, H., Kandori, R., et al. 2005, *PASJ*, **57**, S1
- Elmegreen, B. G. 1989, *ApJ*, **338**, 178
- Esteban, C., García-Rojas, J., Peimbert, M., et al. 2005, *ApJ*, **618**, L95
- Feigelson, E. D., Broos, P., Gaffney, J. A., III, et al. 2002, *ApJ*, **574**, 258
- Ferrière, K. M. 2001, *Rev. Mod. Phys.*, **73**, 1031
- Flower, D. R. 2001, *J. Phys. B: At., Mol. Opt. Phys.*, **34**, 2731
- Froebrich, D., & Rowles, J. 2010, *MNRAS*, **406**, 1350
- Gaisser, T. K., & Schaefer, R. K. 1992, *ApJ*, **394**, 174
- Glover, S. C. O., Federrath, C., Mac Low, M.-M., & Klessen, R. S. 2010, *MNRAS*, **404**, 2
- Gordon, M. A. 1969, *ApJ*, **158**, 479
- Grenier, I. A., Casandjian, J.-M., & Terrier, R. 2005, *Science*, **307**, 1292
- Hirota, T., Bushimata, T., Choi, Y. K., et al. 2007, *PASJ*, **59**, 897
- Hollenbach, D. J., Takahashi, T., & Tielens, A. G. G. M. 1991, *ApJ*, **377**, 192
- Ikeda, M., Oka, T., Tatematsu, K., Sekimoto, Y., & Yamamoto, S. 2002, *ApJ*, **139**, 467
- Kalberla, P. M. W., Burton, W. B., Hartmann, D., et al. 2005, *A&A*, **440**, 775
- Kalberla, P. M. W., McClure-Griffiths, N. M., Pisano, D. J., et al. 2010, *A&A*, **521**, A17
- Kamae, T., Karlsson, N., Mizuno, T., Abe, T., & Koi, T. 2006, *ApJ*, **647**, 692 (erratum, 662, 779 [2007])
- Kavars, D. W., Dickey, J. M., McClure-Griffiths, N. M., Gaensler, B. M., & Green, A. J. 2003, *ApJ*, **598**, 1048
- Kim, M. K., Hirota, T., Honma, M., et al. 2008, *PASJ*, **60**, 991
- Kopp, M., Roueff, E., & Pineau des Forêts, G. 2000, *MNRAS*, **315**, 37
- Krčo, M., Goldsmith, P. F., Brown, R. L., & Li, D. 2008, *ApJ*, **689**, 276
- Kutner, M. L., & Leung, C. M. 1985, *ApJ*, **291**, 188
- Lee, J.-J., Koo, B.-C., Yun, M. S., et al. 2008, *AJ*, **135**, 796
- Lee, S.-H., Kamae, T., Baldini, L., et al. 2011, *Astropart. Phys.*, **35**, 211
- Liszt, H. S. 2006, *A&A*, **458**, 507
- Liszt, H. S. 2007, *A&A*, **476**, 291
- Lombardi, M., & Alves, J. 2001, *A&A*, **377**, 1023
- Maddalena, R. J., Morris, M., Moscowitz, J., & Thaddeus, P. 1986, *ApJ*, **303**, 375
- Magnani, L., Blitz, L., & Wouterloot, J. G. A. 1988, *ApJ*, **326**, 909
- Magnani, L., Chastain, R. J., Kim, H. C., et al. 2003, *ApJ*, **586**, 1111
- Maloney, P., & Black, J. H. 1988, *ApJ*, **325**, 389
- Mengel, M., De Luca, F. C., & Herbst, E. 2001, *Can. J. Phys.*, **79**, 589
- Menten, K. M., Reid, M. J., Forbrich, J., & Brunthaler, A. 2007, *A&A*, **474**, 515
- Mohan, R., Dwarakanath, K., & Srinivasan, G. 2004a, *JA&A*, **25**, 143
- Mohan, R., Dwarakanath, K., & Srinivasan, G. 2004b, *JA&A*, **25**, 185
- Mori, M. 2009, *Astropart. Phys.*, **31**, 341
- Murthy, J., Sahnou, D. J., & Henry, R. C. 2005, *ApJ*, **618**, L99
- Nolan, P. L., Abdo, A., Ackermann, M., et al. 2012, *ApJS*, **199**, 31
- O'Dell, C. R. 2001, *ARA&A*, **39**, 99
- Orlando, E., & Strong, A. W. 2008, in *Proc. 30th Int. Cosmic Ray Conference (July 3–11, 2007 Mérida, Yucatán, Mexico)*, ed. R. Caballero et al. (Universidad Nacional Autónoma), **505** (arXiv:0709.3841)
- Porter, T. A., Moskalenko, I. V., Strong, A. W., Orlando, E., & Bouchet, L. 2008, *ApJ*, **682**, 400
- Prisinzano, L., Micela, G., Flaccomio, E., et al. 2008, *ApJ*, **677**, 401
- Rowles, J., & Froebrich, D. 2009, *MNRAS*, **395**, 1640
- Sanders, D. B., Solomon, P. M., & Scoville, N. Z. 1984, *ApJ*, **276**, 182
- Sandstrom, K. M., Peek, J. E. G., Bower, G. C., Bolatto, A. D., & Plambeck, R. L. 2007, *ApJ*, **667**, 1161
- Schlegel, D. J., Finkbeiner, D. P., & Davis, M. 1998, *ApJ*, **500**, 525
- Sheffer, Y., Rogers, M., Federman, S. R., et al. 2008, *ApJ*, **687**, 1075
- Shepler, B. C., Yang, B. H., Dhillip Kumar, T. J., et al. 2007, *A&A*, **475**, L15
- Snow, T. P., & McCall, B. J. 2006, *ARA&A*, **44**, 367
- Strong, A. W., Bloemen, J. B. G. M., Dame, T. M., et al. 1988, *A&A*, **207**, 1
- Strong, A. W., & Moskalenko, I. V. 1998, *ApJ*, **509**, 212
- Strong, A. W., Moskalenko, I. V., & Reimer, O. 2000, *ApJ*, **537**, 763
- Taylor, S. D., Hartquist, T. W., & Williams, D. A. 1993, *MNRAS*, **264**, 929
- van Dishoeck, E. F., & Black, J. H. 1986, *ApJS*, **62**, 109
- van Dishoeck, E. F., & Black, J. H. 1988, *ApJ*, **334**, 771
- Wall, W. F. 2007, *MNRAS*, **375**, 278
- Wernli, M., Valiron, P., Faure, A., et al. 2006, *A&A*, **446**, 367
- Wilson, B. A., Dame, T. M., Masheder, M. R. W., & Thaddeus, P. 2005, *A&A*, **430**, 523
- Wilson, C. D. 1995, *ApJ*, **448**, L97
- Wolfire, M. G., Hollenbach, D., & McKee, C. F. 2010, *ApJ*, **716**, 1191